# The Frictional-Viscous Transition in Experimentally Deformed Granitoid Fault Gouge

**W. Zhan[1], A. R. Niemeijer[2], A. Berger[1], N. Nevskaya[1], C. J. Spiers[2], M. Herwegh[1]**

[1]Institute of Geological Sciences, University of Bern, Bern, Switzerland.

[2]Department of Earth Sciences, Utrecht University, Utrecht, the Netherlands.

Corresponding author: Weijia Zhan (weijia.zhan@unibe.ch)

**Key Points:**

- The frictional-viscous transition in granitoid gouges is promoted by increasing temperature and decreasing velocity.
- The transition involves forming a dense, ultrafine-grained principal slip zone where dissolution-precipitation creep operates.
- This temperature-, rate- and grain size-sensitive creep mechanism greatly weakens the crust at depth >7 km depending on geothermal gradient.

## Abstract

In crustal faults dominated by granitoid gouges, the frictional-viscous transition marks a significant change in strength constraining the lower depth limit of the seismogenic zone. Dissolution-precipitation creep (DPC) may play an important role in initiating this transition, especially within polymineralic materials. Yet, it remains unclear to what extent DPC contributes to the weakening of granitoid gouge materials at the transition. Here we conducted sliding experiments on wet granitoid gouges to large displacement (15 mm), at an effective normal stress and pore fluid pressure of 100 MPa, at temperatures of 20-650°C, and at sliding velocities of 0.1-100 μm/s, which are relevant for earthquake nucleation. Gouge shear strengths were generally ~75 MPa even at temperatures up to 650°C and at velocities > 1 μm/s. At velocities ≤ 1 μm/s, strengths decreased at temperatures ≥ 450°C, reaching a minimum of 37 MPa at the highest temperature and lowest velocity condition. Microstructural observations showed that, as the gouges weakened, the strain localized into thin, dense, and ultrafine-grained (≤ 1 μm) principal slip zones, where nanopores were located along grain contacts and contained minute biotite-quartz-feldspar precipitates. Though poorly constrained, the stress sensitivity exponent *n* decreased from ≥17 at 20°C to ~2 at 650°C at the lowest velocities. These findings suggest that high temperature, slow velocity and/or small grain sizes promote DPC-accommodated granular flow over cataclastic frictional granular flow, leading to the observed weakening and strain localization. Field observations together with extrapolation suggest that DPC-induced weakening occurs at depths of 7-20 km depending on geothermal gradient.

## Plain Language Summary

Below the Earth's surface, rocks usually undergo a change in strength and deformation behavior as they reach deeper crustal levels, transitioning from strong and brittle behavior in the upper crust, to weak and viscous near the middle crust. This change, known as the frictional-viscous transition, defines the limit in depth where major earthquakes can occur. Some evidence from nature and laboratory experiments suggest that deformation by dissolution-precipitation creep (DPC or "pressure solution") may play an important role in triggering this transition. However, these assumptions lack adequate verification and comprehensive understanding. Here, we conducted laboratory tests across a wide range of temperatures and deformation rates in order to reconstruct the frictional-viscous transition in granitoid rocks, one of the most common rock type in the upper to middle continental crust. We found that granitoid gouges started to weaken and became viscous when being deformed

at higher temperatures and lower deformation rates. As the rock became weaker, deformation localized in a distinct layer called the principal slip zone. This is very fine-grained and contains tiny pores filled with many newly precipitated minerals, which proves active DPC. In nature, activation of DPC could trigger the frictional-viscous transition at shallower crustal depths than otherwise expected.

## 1 Introduction

Granitoid or granitic fault gouge is a type of non-cohesive fault rock that consist predominantly of quartz, albite and orthoclase (Barbarin, 1999; Sammis et al., 1987). Observations of natural fault zones suggest deformation often localizes into a thin layer of non-cohesive granitoid fault rocks in the crystalline part of the continental crust, at upper to middle crustal depths (Baumberger et al., 2022; Berger et al., 2017; Wehrens et al., 2016). Therefore, the mechanical behavior of these granitoid gouges is highly relevant for determining the rheology of crustal fault zones. The frictional-viscous transition in these gouges is of great importance, as it not only marks a pronounced change in rheological properties of the Earth’s lithosphere, but also helps to constrain the lower boundary of the seismogenic zone, where large-magnitude earthquakes normally originate (Evans et al., 1990; Scholz, 1998; Sibson, 1982; Tse & Rice, 1986).

In the classical crustal rheological profile, the frictional-viscous transition extends over a depth range of several kilometers, serving as a bridge between predominantly frictional behavior in the upper crust and viscous behavior in the lower crust (Bürgmann & Dresen, 2008; Burov, 2011; Goetze & Evans, 1979; Kohlstedt et al., 1995; Paterson & Wong, 2005). The strength of the upper crust typically increases linearly with depth, characterized by a constant slope represented by friction coefficients of ~0.6-0.85, often referred to as Byerlee's law (J. Byerlee, 1978; Labuz & Zang, 2012). Within the upper crust, frictional sliding occurs along preexisting fault planes, with low temperature and strain rate sensitivity. In contrast, the strength of the lower crust generally decreases with increasing depth. This behavior is often described by the thermally activated, power-law flow of monomineralic quartz or feldspar, which are the most abundant rock forming minerals at this crustal level. In the case of these end-member minerals, deformation is thought to be mainly controlled by dislocation creep and dynamic recrystallization processes (Rutter & Brodie, 2004b; Rybacki & Dresen, 2004). Deformation at the frictional-viscous transition is usually considered as a combination of the frictional and creep mechanisms that separately govern the deformation of the upper and the lower crust. However, the widespread occurrence of stylolites, slickenfibres, veining, grain scale overgrowths and truncated grain-grain contacts, found in exhumed mid-crustal fault zones (Gratier et al., 2023; Hickman et al., 1995; Wassmann & Stöckhert, 2013, and references therein), indicate that apart from the classical frictional and creep mechanisms, dissolution-precipitation creep may play an important role particularly in the case of polymineralic faults. It is also known as pressure solution (Gratier et al., 2013; Spiers et al., 1990) or viscous granular creep (Paterson 1995; Stünitz 1998).

Dissolution-precipitation creep (DPC) is a fluid-assisted deformation mechanism involving three processes: first, material is dissolved at grain contacts with relatively high normal stress concentrations, then transported away from the contacts by diffusive mass transport process, and finally precipitated at low stress sites (Gratier et al., 2013; Rutter, 1983; X. Zhang & Spiers, 2005). Under conditions where fluids are present, DPC is promoted and accelerated by the presence of fine grain size, polymineralic composition, moderate temperatures and slow strain rates (de Meer & Spiers, 1997; Rutter, 1983; Visser et al., 2012). These conditions align well with those found in permeable mid-crustal fault zones, suggesting that DPC may indeed represent a dominant deformation mechanism within the frictional-viscous transition. DPC is typically known to play a crucial role in compaction, sealing and healing of fault rocks during the interseismic period between individual earthquake events (Nakatani & Scholz, 2004; Niemeijer et al., 2002; Schwichtenberg et al., 2022). More importantly, several studies have demonstrated that this mechanism may also reduce the strength of fault rocks at the frictional-viscous transition, especially in fault rocks that contain fine-grained phyllosilicates (Bos & Spiers, 2001; Kirkpatrick et al., 2021) or albite (Okuda et al., 2023). Yet, it remains unclear to what extent DPC contributes to the weakening of granitoid gouge materials at the frictional-viscous transition.

Many laboratory experiments conducted under hydrothermal conditions have investigated the frictional-viscous transition and associated deformation processes in the case of different rock compositions, such as pure quartz gouge (Hirth & Tullis, 1992, 1994), albite gouge (Tullis & Yund, 1992), and granitoids (Blanpied et al., 1995; Lei, Niemeijer, et al., 2022; Mitchell et al., 2016; Simpson, 1985; Tullis & Yund, 1980). These experimental studies have demonstrated that the frictional-viscous transition occurs in a range of increasing temperature and/or decreasing sliding velocity, which typically is expressed by temperatures of around 350-450°C under a velocity range of 0.01-1 μm/s. For monomineralic aggregates such as quartz gouge, DPC has been demonstrated to play an important role in weakening the gouges (Niemeijer et al., 2008). A more pronounced weakening effect was observed in granitoid gouges due to the addition of water, emphasizing the important role of fluid-assisted deformation mechanisms, such as DPC, in initiating the frictional-viscous transition in polymineralic aggregates (Blanpied et al., 1995; Griggs, 1967; Tullis & Yund, 1980). However, these experiments were confined to small shear strains ($\gamma \approx$ 4-7), and the microstructural investigations were limited to either optical microscopy or transmission electron microscopy scales. These constraints hinder a comprehensive understanding of the role of DPC on weakening at the frictional-viscous transition, as its processes are mainly observable at intermediate grain-scales.

In this study, we aim to replicate the frictional-viscous transition in the case of fine-grained granitoid gouges in order to gain more profound knowledge of the associated deformation mechanisms. We conducted sliding experiments on wet granitoid gouges to large displacement (15 mm) under hydrothermal conditions (20-650°C, 100 MPa pore fluid pressure, and effective normal stress) and at sliding velocities (0.1-100 μm/s) relevant for earthquake nucleation. Microstructures of deformed samples were quantitatively analyzed at a variety of scales, using methods allowing observation from the mm down to the nm range. The laboratory measurements of gouge strengths were further extrapolated to natural conditions. Together, our results demonstrate that notable weakening at the frictional-viscous transition is accompanied by intense strain localization, elimination of fracture arrays and the formation of nanopores at grain contact surfaces that contained tiny precipitated biotite flakes. In terms of deformation mechanisms, cataclastic frictional granular flow is gradually replaced by DPC-accommodated viscous granular flow at temperatures above 450°C, sliding velocities below 1 μm/s, and/or mean grain size below 1 μm.

## 2 Materials and Methods

### 2.1. Starting material

The investigated “gouges” were produced from a granitoid ultramylonite that was drilled and cored from a ductile shear zone inside the Nagra Grimsel Test Site (GTS), an underground rock laboratory located near Grimsel Pass in the Aar Massif, Central Switzerland (46°35'27''N, 8°19'17''E; e.g. Schneeberger et al., 2017). The collected sample was disaggregated in a step-wise procedure to simulate non-cohesive gouge-like powders. They were first crushed into large fragments by electrical fragmentation, which is based on high-voltage discharges (SELFRAG®: www.selfrag.com; Giese et al., 2010; Zwingmann et al., 2017), then further milled into powders with a McCrone micronizing mill for less than 1 minute (Behnsen & Faulkner, 2011). Fragments that remained large were manually ground with a mortar and pestle and subsequently wet sieved to obtain a grain size fraction smaller than 125 μm. All of the disaggregated material was collected and dried in an oven at ~40°C for at least 48 h and stored in sealed containers at room temperature and ambient humidity.

To determine the mineralogical composition and particle size distribution, powders were analyzed using X-ray Powder Diffraction (XRD) and a laser particle-size diffractometer, respectively (supporting information, Text S1). XRD results show that the starting material has a typical granitoid composition, being composed of quartz (37 wt.%), albite (38 wt.%), orthoclase (11 wt.%), biotite (8 wt.%) and epidote (6 wt.%). Particle size analysis shows a log-normal distribution, with a mean grain size of 56 μm and a standard deviation of 47 μm.

### 2.2. Experimental techniques

Rock deformation experiments were conducted in a hydrothermal ring shear apparatus, installed at the HPT lab at Utrecht University (see details in den Hartog et al., 2012; Niemeijer et al., 2008). In this apparatus, an internally heated pressure vessel and a rotary drive system are installed inside an Instron loading frame (Figure 1a). Within the pressure vessel, the pore fluid pressure is controlled using a hand pump. The added fluid is deionized water. The effective normal stress (resolution ±0.05 MPa) is transmitted to the sample through a pressure-compensated loading piston using the Instron ram (Figure 1a). The sample is heated to the desired temperature (resolution ±0.5°C) using a coiled thermocoax furnace surrounding the sample-piston assembly. Sample temperatures are measured using a K-type thermocouple installed ~5 mm away from the sample layer. For each experiments, a ~1.5 mm thick gouge layer was sandwiched between two internal René-41® superalloy pistons in the sample-piston assembly (Figure 1c). The internal pistons are roughened with ~0.2 mm deep, cross-cut grooves to increase the grip between the sample powder and piston surfaces (Figure 1d). The gouge is confined with inner (22 mm diameter) and outer confining rings (28 mm diameter) which were coated with Molykote® ($MoS_2$) antifriction lubricant to reduce the wall friction between sample and the confining rings (Verberne et al., 2015). The resulting shear stress is externally measured using the torque gauges mounted on the torque bar at the top of the pressure vessel (resolution ±0.006 MPa). Shear displacement is measured using a potentiometer installed at the bottom-forcing block (resolution ±0.001 mm).

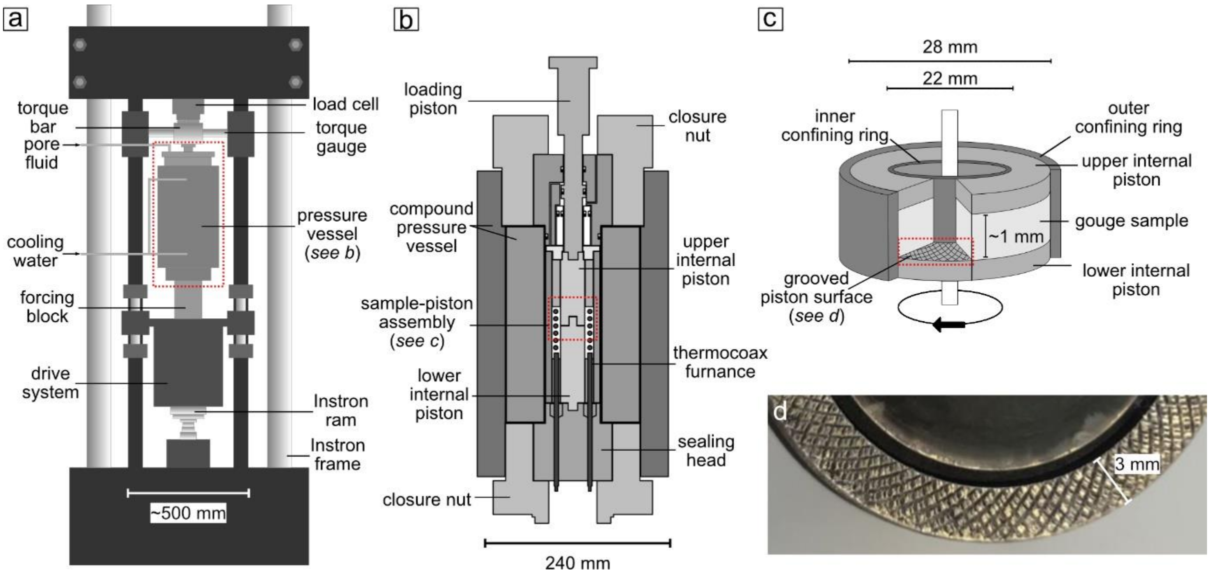


**Figure 1**. (a) Schematic diagram of hydrothermal ring shear apparatus showing the pressure vessel and fluid lines; (b) Cross section of the compound pressure vessel, modified after den Hartog and Spiers (2013); (c) Schematic diagram of sample assembly; (d) Photograph of the grooved piston surface.

In each experiment, the desired temperature and pore fluid pressure were applied within ~30 min of installing the sample in the apparatus. After equilibrating for at least 45 min, the effective normal stress was applied to the sample, and then the rotary driving system was switched on. Upon completion of the experiment, shear stress, effective normal stress, temperature, and pore fluid pressure were sequentially decreased. Temperature and pore fluid pressure were adjusted to atmospheric conditions in a stepwise procedure to avoid pore fluid boiling. The experiment termination process took ~30 min. During the experiment, signals including shear displacement, torque, temperature, axial displacement and load, pore fluid pressure, and rotational drive velocity were continuously recorded using a 18-bit A/D converter and an acquisition rate of 900 Hz, which was averaged and logged at frequencies of 1-100 Hz, depending on sliding velocities.

Sixteen experiments in total were conducted at an effective normal stress of 100 MPa and a pore fluid pressure of 100 MPa applying ~15 mm displacement (shear strain of ~23). They are subdivided into three groups based on the applied sliding velocities of $V$ = 100, 1, 0.1 μm/s (Table 1). In the first group, gouges were sheared at a constant sliding velocity of $V$ = 100 μm/s and temperatures ranging from 20°C to 650°C, in order to study the effect of temperature on the strength of the gouge. The second and the third groups are identical to the first group, except that the applied sliding velocity was, respectively, set at $V$ = 1 μm/s and $V$

= 0.1 μm/s to study how fault slip rate influences the strength of gouge samples. To prevent melting, the highest temperature and pore fluid pressure conditions explored were deliberately chosen to be well below the $H_2O$-saturated melting curve for granitoid system (T= 690°C at 200 MPa, Johannes, 1984; Lamadrid et al., 2014). After reaching the desired displacement, each sample was quickly removed from the apparatus and dried in an oven. In some experiments, samples underwent shearing and were then held at the designated temperature and pressure for a specific duration (listed as $t_{hold}$ in Table 1), followed by unloading. Static grain growth of grains during the hold duration may influence microstructures, particularly the absolute grain sizes of sheared samples. To investigate these effects, we conducted additional experiments with identical displacement, sliding velocity and zero hold duration ($t_{hold}$ = 0 h).

During data processing, the recorded torque was corrected for seal friction to obtain the shear stress ($\tau$), while the potentiometer displacement (D) was corrected for elastic distortion. We define the yield point as the point of the minimum second derivative of the shear stress-displacement curve. In the initial loading stage leading up to the yield point thus defined, shear stresses showed a near-linear increase with displacement, appearing as a straight line in the stress-displacement curve. Beyond the yield point, the rate of increase in shear stresses decreased, i.e. the slope of the stress-displacement curves decreases, ultimately approaching a steady state. The yield point shear stresses ($\tau_{yd}$) were calculated as the average of measurements taken over a 1 mm displacement interval beyond the yield point displacement value. The (near) steady-state shear stresses ($\tau_{ss}$) were calculated in a similar way, but only when a total displacement of 15 mm was achieved. For experiment u1150 with a total displacement less than 15 mm, $\tau_{ss}$ was picked up at a displacement of ~ 13 mm. The difference between $\tau_{ss}$ and $\tau_{yd}$ represents the extent of shear stress changes ($\Delta\tau$), calculated as $\Delta\tau = \tau_{ss} - \tau_{\mathrm{yd}}$.

**Table 1.** List of experiments, conditions and key data. All experiments were conducted under an effective normal stress of 100 MPa and a pore fluid pressure of 100 MPa (normal stress is 200 MPa). $T$: temperature, $V$: sliding velocity, $D$: displacement, $t_{hold}$: time for sample being hold at applied P-T conditions before unload, $\tau_{yd}$: yield point shear stress selected at the point of the minimum second derivative of shear stress-displacement curve, $\tau_{ss}$: (near)

steady-state shear stress selected at displacements of ~15 mm, $\Delta\tau = \tau_{ss} - \tau_{yd}$, $\mu_{ss}$: apparent friction coefficient at (near) steady-state, calculated as $\mu_{ss} = \tau_{ss}/\sigma_n^{eff}$ by ignoring cohesion.

| Experiments | $T$ (°C) | $V$ (μm/s) | $D$ (mm) | $t_{hold}$ (h) | $\tau_{yd}$ (MPa) | $\tau_{ss}$ (MPa) | $\Delta\tau$ (MPa) | $\mu_{ss}$ (-) |
|---|---|---|---|---|---|---|---|---|
| $V$ = 100 $\mu m/s$ | | | | | | | | |
| u1051 | 20 | 100 | 15.08 | 0.0 | 56.69 | 74.50 | 17.81 | 0.75 |
| u1049 | 200 | 100 | 15.11 | 1.4 | 65.01 | 73.58 | 8.57 | 0.74 |
| u1052 | 450 | 100 | 15.10 | 1.1 | 59.96 | 77.40 | 17.44 | 0.77 |
| u1059 | 650 | 100 | 15.47 | 0.5 | 54.81 | 81.51 | 26.70 | 0.82 |
| $V$ = 1 $\mu m/s$ | | | | | | | | |
| u1038 | 20 | 1 | 15.98 | 10.0 | 68.97 | 81.11 | 12.14 | 0.81 |
| u908 | 200 | 1 | 15.60 | 0.0 | 56.60 | 75.41 | 18.81 | 0.75 |
| u909 | 450 | 1 | 15.10 | 0.1 | 57.79 | 73.04 | 15.25 | 0.73 |
| u1154 | 650 | 1 | 16.25 | 0.0 | 59.61 | 67.83 | 8.22 | 0.68 |
| u913 | 650 | 1 | 15.60 | 12.0 | 64.34 | 49.78 | -14.56 | 0.50 |
| u1060 | 650 | 1 | 17.10 | 41.9 | 62.03 | 63.94 | 1.91 | 0.64 |
| $V$ = 0.1 $\mu m/s$ | | | | | | | | |
| u1157 | 20 | 0.1 | 15.59 | 0.0 | 56.31 | 65.82 | 9.51 | 0.66 |
| u1153 | 200 | 0.1 | 15.49 | 0.0 | 54.56 | 65.84 | 11.28 | 0.66 |
| u1151 | 450 | 0.1 | 15.50 | 0.0 | 68.73 | 73.56 | 4.83 | 0.74 |
| u1150 | 650 | 0.1 | 13.10 | 0.0 | 73.21 | 49.70 | -23.51 | 0.50 |
| u1175 | 650 | 0.1 | 15.49 | 2.0 | 63.73 | 43.08 | -20.65 | 0.43 |
| u910 | 650 | 0.1 | 19.80 | 9.6 | 60.09 | 37.27 | -22.82 | 0.37 |

### 2.3. Analytical methods

At the end of each experiment, we obtained a ring-shaped gouge layer with dimensions of ~3 mm in width and ~0.7 mm in thickness. Upon drying and disassembling, the deformed gouges often split into several fragments. We carefully selected relatively thick fragments for microstructural imaging, assuming their microstructures are representative of the entire sample. The fragments from each experiment were subjected to two different treatments: some were air-impregnated with an epoxy resin, while others were fixed to carbon SEM stubs with no impregnation. For the air-impregnated samples, sectioning was performed in a plane normal to the shear plane and ~2 mm tangential to the centrally inscribed circle (22 mm diameter), followed by a 10 nm thick carbon coating. Microstructural consistency was confirmed across different sectioned distances from the inscribed circle. Backscatter images of the sectioned sample were collected and stitched using a ZEISS EVO 50 scanning electron microscope (SEM) at 20 kV and 0.5-1.5 nA. These stitched images provided an overview of the microstructure with the aim to cover the entire thickness of the final gouge layer. Close-up images were obtained using a ZEISS Gemini SEM 450 (FEG-SEM) operating at 10 kV and 300 pA. As for the fragments on carbon SEM stubs, backscatter images of broken surfaces were obtained using the FEG-SEM operating at 5 kV and 100 pA to enable investigation of grain boundary morphologies.

BSE images were processed using the interactive machine-learning tool ilastik, and then quantitatively analyzed using ImageJ. A summary of image analysis workflow can be found in Text S2 of the supporting information. Based on the processed images, we classified four distinct objects types: 'clasts', 'matrix', 'pores' and 'cracks'. 'Clasts' refers to particles larger than 1 $\mu m^2$ (~120 pixel$^2$), while 'matrix' refers to all particles smaller than 1 $\mu m^2$. 'Pores' are isolated openings, and 'cracks' refers to interconnected (sub)planar openings, which presumably resulted from the unloading of the experiments. Two microstructural features were quantitatively characterized, including the grain size distribution of clasts, as well as the relative area proportion between clast, matrix and porosity (also referred to as clast:matrix:porosity ratio). For the grain size distribution, the area-weighted diameter ($d_i, \mu m$) was calculated using the measured area ($A_i, \mu m^2$) of each clast, according to the formula below (Berger et al., 2011):

$$d_i = 2 * \sqrt{\frac{A_i}{\pi}} \quad (1)$$

## 3 Results

### 3.1. Mechanical data

Diagrams of shear stress ($\tau$) against displacement ($D$) are shown in Figure 2 for different sliding velocities ($V$ = 100, 1, 0.1 μm/s) and temperatures ($T$ = 20, 200, 450, 650°C). Despite some variability, all experiments showed a steep, near-linear increase in shear stress, reaching the yield point at $\tau_{yd}$ = ~70 MPa within the first 1-2 mm displacements. As displacements continued, shear stresses either increased (displacement-hardening) or started to decrease (displacement-weakening) until gradually approaching steady state ($\tau_{ss}$). The extent of shear stress changes ($\Delta\tau$) between yield point and the steady state varied from a negative change of $\Delta\tau$ = -24 MPa for samples that underwent displacement weakening, to a positive change of $\Delta\tau$ = +27 MPa for those with displacement hardening. Both the applied temperatures and sliding velocities influenced the sign of shear stress changes (displacement-hardening or displacement-weakening), the extent of shear stress changes ($\Delta\tau$), as well as the stability of sliding (stable or unstable). Aforementioned key data are listed in Table 1.

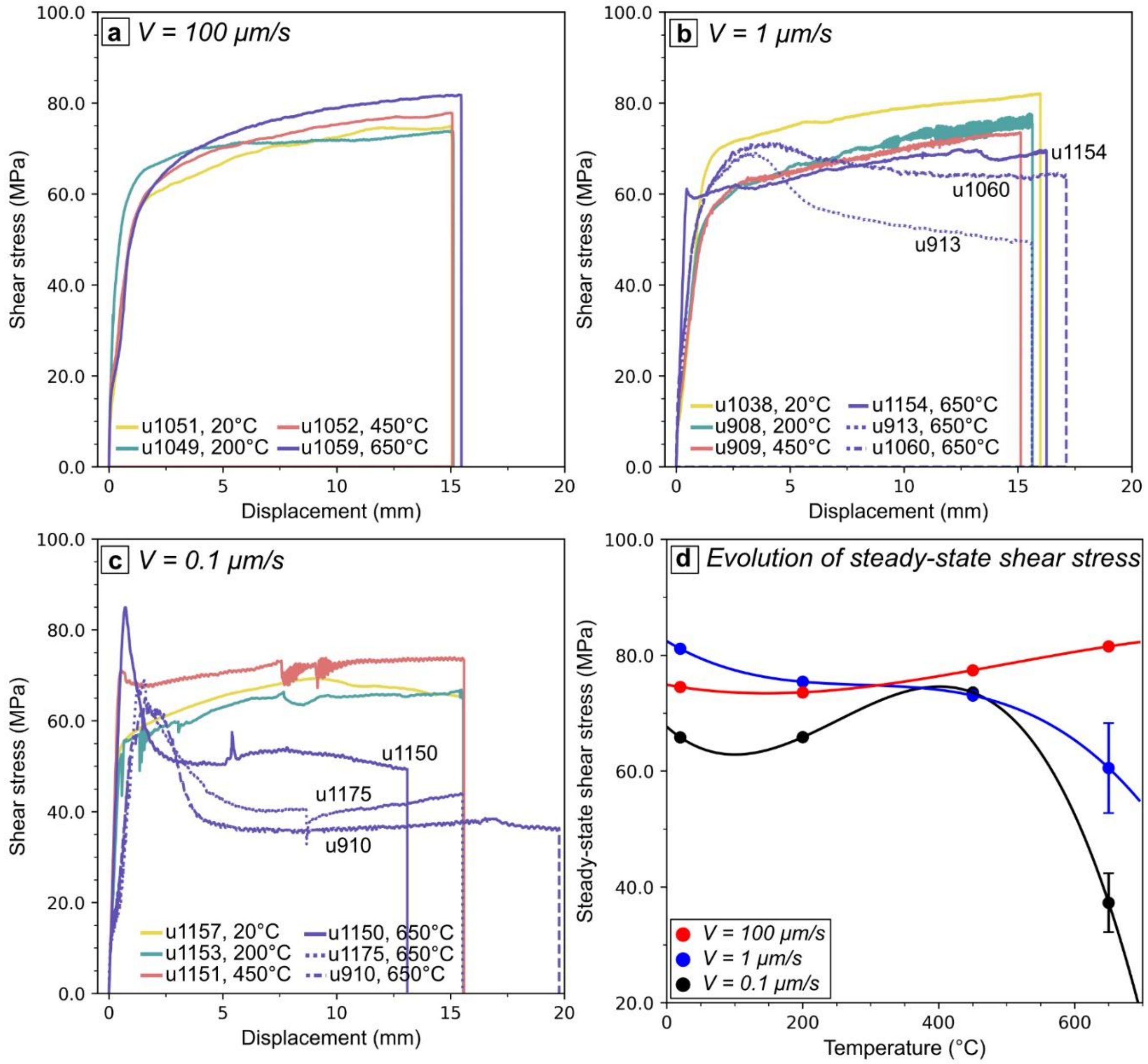


**Figure 2.** Plots of shear stress ($\tau$) against shear displacement ($D$), showing data from experiments at (a) $V$ = 100 μm/s, (b) $V$ = 1 μm/s, and (c) $V$ = 0.1 μm/s. See Table 2 for a list of conditions applied in these experiments. (d) Steady-state shear stress ($\tau_{ss}$) plotted as a function of temperature ($T$) and sliding velocity ($V$). Lines are interpreted trends.

In the case of gouges sheared at a sliding velocity of $V$ = 100 μm/s, samples sheared at various temperatures consistently showed stable sliding, continuous displacement-hardening, eventually reaching $\tau_{ss}$ = ~75 MPa (Figure 2a). The extent of shear stress increase exhibited no discernible dependency on temperature. In comparison, for gouges subjected to a medium sliding velocity of $V$ = 1 μm/s, temperatures showed a pronounced influence on the type of shear stress changes and the stability of sliding (Figure 2b). At lower temperatures of $T$ = 20-450°C and in one experiment (u1154) at $T$ = 650°C, these samples were characterized by displacement-hardening with $\tau_{ss}$ = ~75 MPa. As temperatures increased to $T$ = 650°C, the samples showed a distinctive behavior, with a short region of displacement-hardening in the first 2 mm displacement, followed by displacement-weakening towards $\tau_{ss}$ = ~50-64 MPa. Only experiments conducted at temperatures between 200 and 450°C showed unstable sliding behavior, which often occurred as stick-slip events. In comparison, gouges subjected to slow shearing at $V$ = 0.1 μm/s exhibited a temperature-dependent behavior similar to those sheared at $V$ = 1 μm/s. However, for those sheared at $T$ = 650°C, $\tau_{ss}$ was ~37-50 MPa and a shorter critical displacement (1-3 mm) was needed for the transition from displacement-hardening to weakening behavior (Figure 2c). Note that the limited reproducibility of experiments conducted at $T$ = 650°C and $V$ = 0.1-1 μm/s is probably caused by fluctuations in pore fluid pressure applied during experiments (see supporting information Figure S3).

To highlight the influence of temperature and sliding velocity on the strength of the granitoid gouge, we plot the steady-state shear stress ($\tau_{ss}$) against temperature in Figure 2d for the three investigated sliding velocities ($V$ = 100, 1, 0.1 μm/s). Gouges sheared at $V$ = 100 μm/s showed consistently high steady-state shear stresses that progressively increased with elevated temperatures, from $\tau_{ss}$ = 74 MPa at 20°C to $\tau_{ss}$ = 82 MPa at 650°C. In contrast, gouges sheared at lower velocities of $V$ = 1 and 0.1 μm/s exhibited mostly temperature-insensitive shear stresses at $T \leq$ 450°C but showed significant weakening at $T$ = 650°C. Specifically, for gouges sheared at $V$ = 1 μm/s, shear stresses ranged from 73-81 MPa at $T \leq$ 450°C, dropping to ~60 MPa at $T$ = 650°C (weakening by ~16%). In comparison, gouges sheared at $V$ = 0.1 μm/s showed a lager reduction in shear stresses, going from 74 MPa at 450°C to ~43 MPa at 650°C (weakening by ~42%). Overall, in our experiments, the displacement-weakening and a notable reduction in steady-state shear stress occurred at $T \geq$ 450°C and $V \leq$ 1 μm/s. Once the weakening was triggered, lower sliding velocities led to greater weakening over shorter critical displacements, ultimately resulting in lower steady-state shear stresses.

### 3.2. Microstructures

The mechanical data showed that considerable weakening occurred in granitoid gouge as temperature increased and sliding velocity decreased. To understand the evolution of the deformation processes during the transition from strong to weak gouges, we adopted a three-step microstructural analysis. First, we used quantitative image analysis to systematically categorize the strain localization consistently observed in the sheared gouges. Then, we seperately examined the effect of temperature and velocity on the microstructural evolution of the whole gouge layer, by analyzing two experimental series with controlled velocity/temperature conditions. Finally, we analyzed the grain-scale microstructural evolution in two end-member cases: the strongest and the weakest gouges.

### 3.2.1. Strain localization in the deformed gouges

The microstructures of the sheared gouges were classified into three zones, based on the degree of strain localization: the ‘bulk zone’, the ‘slip zone’ and the ‘principal slip zone’ (PSZ). The evaluation of localization was performed using quantitatively characterized microstructural features, including the grain size distribution of clasts, and the clast:matrix:porosity ratio (see definition in section 2.3). Notably, in zones with a higher degree of strain localization, additional particles that were initially clasts were incorporated into the fine-grained matrix. This led to a narrower grain size distribution of clasts and a reduction in the mean size ($\bar{d}$). Consequently, this process led to a lower clast:matrix ratio, and reduced porosity compared to less localized zones. Table S1 summarizes the width, median, and mean particle size of localized zones of all sheared gouges.

To illustrate the varying degrees of strain localization, we show a quantitative microstructural analysis of the sheared gouge from experiment u913 ($T$ = 650°C, $V$ = 1 μm/s, D ≈ 15 mm) and the starting material (compressed and held at $T$ = 650°C for ~4h) (Figure 3). The starting material showed homogeneously distributed compaction, characterized by densely fractured, coarse-grained clasts, loosely consolidated among fine-grained clasts (Figure 3a). Quantitative analysis revealed a clast size ($d$) that ranged between 1-98 μm with a mean $\bar{d}$ of ~29 μm, while the clast:matrix:porosity ratio was 68%:11%:21%. Owing to shear deformation, sample u913 developed distinct strain localization and pervasive clast size reduction, with a less localized bulk zone in the center, an intermediate localized slip zone, and a highly localized PSZ towards the sample-piston interface (Figure 3b). The bulk zone was characterized by a clast size $d$ ranging from 1-61 μm with a mean $\bar{d}$ ≈ 24 μm and a clast-dominant texture (a clast:matrix:porosity ratio of 71%:29%:9%). In comparison, the slip zone had a narrower $d$ ranging from 1-20 μm with a smaller $\bar{d}$ of ~7 μm, and a higher proportion of matrix (a clast:matrix:porosity ratio of 53%:41%:6%). The PSZ showed the most intense clast size reduction and compaction, resulting in a clast size $d$ ranging from 1-4 μm with a $\bar{d}$ of ~2 μm, and a matrix-dominant texture (a clast:matrix:porosity ratio of 7%:92%:1%). High-magnification FEG-SEM images of PSZs indicated that the mean and median grain size of particles (clasts and matrix) were down to 0.6 μm and 1.2 μm, respectively. This quantitative analysis showed that sheared gouges developed three different microstructural domains, transitioning from the coarse-grained and porous bulk zone, comparable to the unsheared microstructure, to the medium-grained and less porous slip zone, and finally to the ultrafine-grained and dense PSZ. However, it should be noted that not all sheared gouges developed the aforementioned three microstructural domains, and many factors, including temperatures and sliding velocities, affected the level of strain localization. Section 3.2.2 provides a detailed description of these factors.

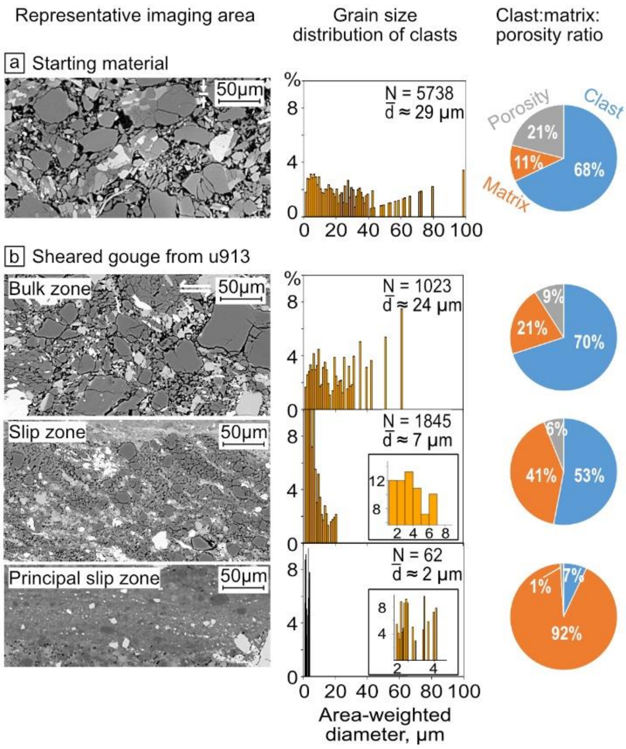


**Figure 3.** Quantitative microstructural analysis of (a) starting material (T = 650°C, V = 0 μm/s, D = 0 mm) and (b) gouge from experiment u913 (T = 650°C, V = 1 μm/s, D ≈ 15 mm), including three zones with varying degrees of deformation localization. Left column: the representative imaging areas cropped from the entire gouge layer. Central column: the grain size distribution of clasts from stitched BSE images. N = count numbers, $\bar{d}$ = the mean diameter. Right column: relative ratio of clasts-matrix-porosity, relative ratio equals to the sum area of each phase divided by the entire imaging area.

### 3.2.2. Microstructural evolution of the whole gouge layer

We chose two experimental series to study the microstructural evolution corresponding to the transition from high to low strength: one with increasing temperature of $T$ = 20°C-450°C-650°C and fixed velocity of $V$ = 1 μm/s (Figure 4a-4c), and the other with decreasing velocity of $V$ = 100-1-0.1 μm/s and fixed temperature of $T$ = 650°C (Figure 4d-4f).

In the first series of experiments, involving increasing temperature, all sheared samples showed some level of strain localization (bulk, slip or principal slip zones), fracture arrays (Y- and R-shears) and P-foliations (following terminology used by Logan et al., 1992; Passchier & Trouw, 1996). P-foliations were defined by alternating layers of well-aligned biotite and sigmoidal porphyroclasts of orthoclase (Figure 4f). The sample sheared at a low temperature (20°C; Figure 4a) showed a bulk zone and a slip zone, with no PSZ observed. The width of the slip zone constituted up to ~39% of the total recovered gouge layer, with a maximum width of ~195 μm (Table S1). Note that the boundaries separating the designated zones were not sharply defined, as transitions in the microstructural features between them occurred gradually. Both bulk and slip zones were dissected by interface-parallel Y-shears and inclined R-shears, which extend continuously up to ~200 μm in length. P-foliations in the slip zones were inclined at relatively low angles of ~30° to the shear plane, compared to ~45° in the bulk zones, indicating that larger shear strain was accommodated in the slip zones. For the sample sheared at an intermediate temperature (450°C; Figure 4b), a highly localized PSZ evolved close to the sample-piston interface, with a width that constituted ~10% of the whole gouge layer (a width of ~83 μm). The continuous intergranular fracture arrays remained pervasive throughout the entire sample. Meanwhile, P-foliations in the slip zone and PSZ became more abundant and exhibited lower angles to the shear plane compared to those sheared at low temperatures in Figure 4a. As for the sample sheared at a high temperature (650°C; Figure 4c), deformation became even more localized, forming an extremely thin PSZ with a width that constituted ~5% of the whole gouge layer (a width of ~42 μm). Continuous intergranular fracture arrays in the slip zone and PSZ were replaced by closely spaced P-foliations orientated subparallel at around 15° to the shear plane.

In comparison with the first series of experiments, the second series exhibited a similar change in microstructural features (Figure 4 right column). At fixed temperature and decreasing velocity, this series of samples showed more localized deformation occurring in PSZs, a reduction in the number of fracture arrays, and an increased intensity of P-foliations, with the predominant orientation aligning at around 15° to the shear plane. In general, all samples in the second series of experiments at high temperature ($T$ = 650°C) displayed only incipient fracture arrays, in contrast to the clear and distinct fracture arrays observed in the first series at lower temperatures $T \leq 450$°C.

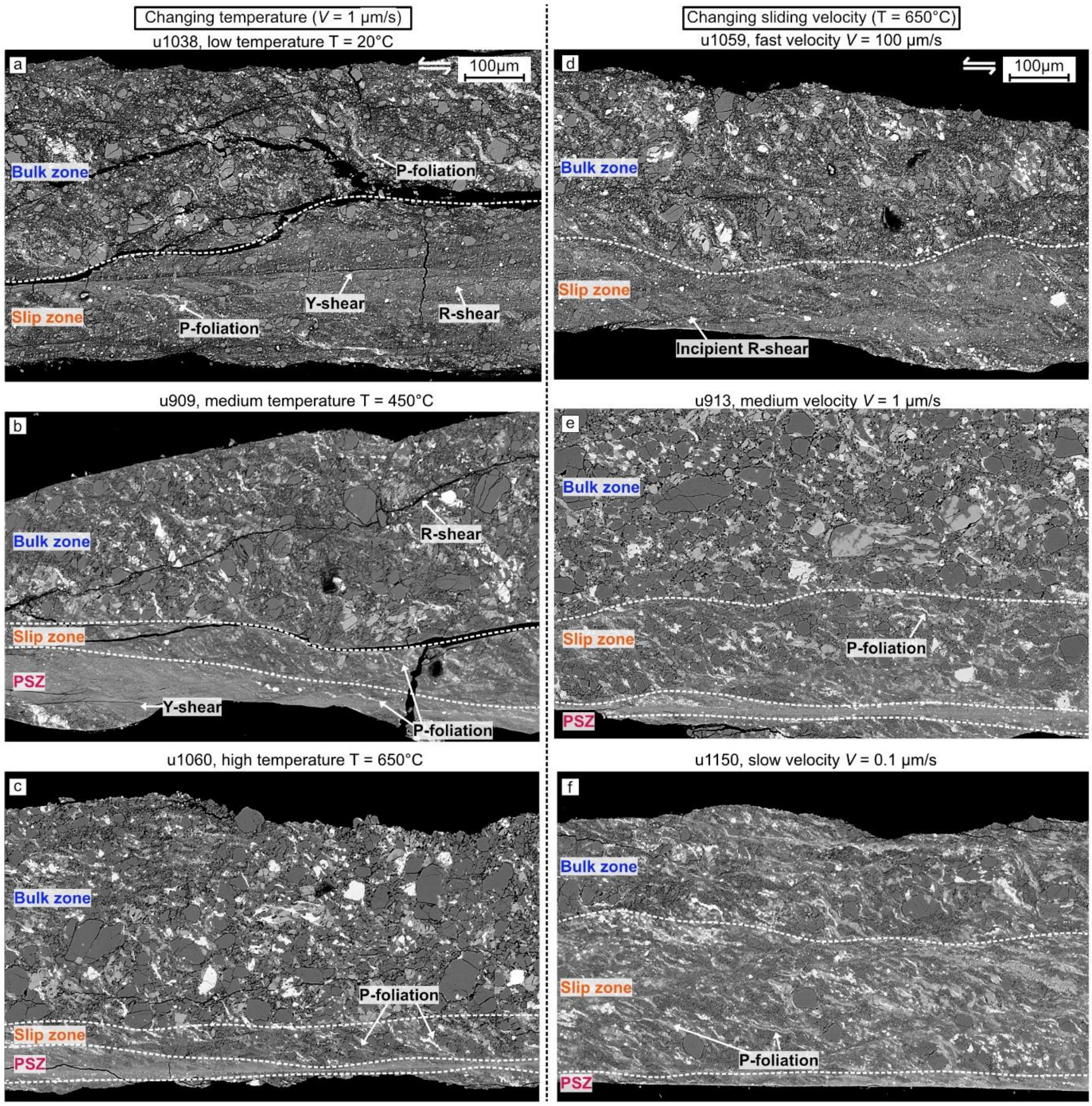


**Figure 4.** Mosaics of backscatter images of the whole gouge layers, showing the effect of temperature (a-c, left column) and sliding velocity (d-f, right column). All samples have the same shear sense and scale bar, as shown in (a) and (d). Note that in the backscatter images, quartz or albite appear as dark grey phases, orthoclase is light grey, biotite or epidote are white phases.

### 3.2.3. Grain-scale microstructural evolution

The observed ultrafine-grained and dense PSZs accommodated most of the total shear strain. To gain an improved understanding of the deformation processes in these localized zones, we conducted high-magnification FEG-SEM imaging on two extreme cases: the strongest (u1051, u1059; Figure 5a-5b) and the weakest gouges (u1150, u910; Figure 5c-5f).

Samples tested in experiments u1051 ($\tau_{ss}$= 75 MPa) and u1059 ($\tau_{ss}$= 82 MPa) exhibited the highest strengths. These samples underwent shearing at the highest velocity of $V$ = 100 μm/s and at $T$ = 20°C and 650°C, respectively. As shown in Figure 5a-5b, a detailed examination of the grain-scale microstructures revealed that the slip zones formed in these strong gouges exhibited clast-dominant gouge textures, where a large volume of fine-grained matrix surrounded fractured angular clasts. The mean grain size of these slip zones was $\bar{d} \approx$ 3-6 μm (Table S1).

Regarding the weak gouges recovered from experiments u1150 ($\tau_{ss}$= 49 MPa) and u910 ($\tau_{ss}$= 37 MPa), these were subjected to the lowest velocity explored ($V$ = 0.1 μm/s) and the highest temperature ($T$ = 650°C). In comparison with the strong gouges, the slip zones showed a marked increase in the proportion of clasts to matrix, with a larger fraction of rounded clasts, plus well-developed P-foliations and truncated grain-to-grain contacts (Figure 5c-5d). Upon closer inspection, it became clear that sigmoidal porphyroclasts of orthoclase, which defined P-foliation at a larger scale, were actually aggregates of many cataclastically fragmented, equidimensional grains that had been smeared into a sigmoidal shape (Figure 5c). Truncated contacts and fluid inclusions were often found within these aggregates (Figure 5c). The PSZs contained sparsely distributed clasts embedded in a dense ultrafine-grained matrix, consisting of well-mixed phases such as quartz and feldspar (Figure 5e-5f). Individual grains were difficult to identify in backscatter electron imaging mode because of grain aggregates being agglutinated together, resulting in low-relief grain boundaries. Semi-quantitative analysis suggested the mean grain size of the PSZs was $\bar{d} \approx$ 0.6-1.1 μm (Table S1). In both slip zones and PSZs, we observed nanometer-sized pores, small biotite flakes and quartz overgrowths on open pore walls (Figure 5g-5h). These nanopores were primarily distributed along the grain contact surfaces (i.e. grain-to-grain boundaries), and sometimes trapped inside grains as fluid inclusions. Their sizes ranged from a few nanometers in diameter in the PSZs (Figure 5h), to larger diameters of up to 1 μm in the slip zones (Figure 5g). Idiomorphic biotite flakes, which were remarkably small, measuring ~ 30 nm in length and 10 nm in width often filled the nanopores. In these biotite flakes, we found no evidence for grain deformation, such as folding or kinking on the basal slip plane.

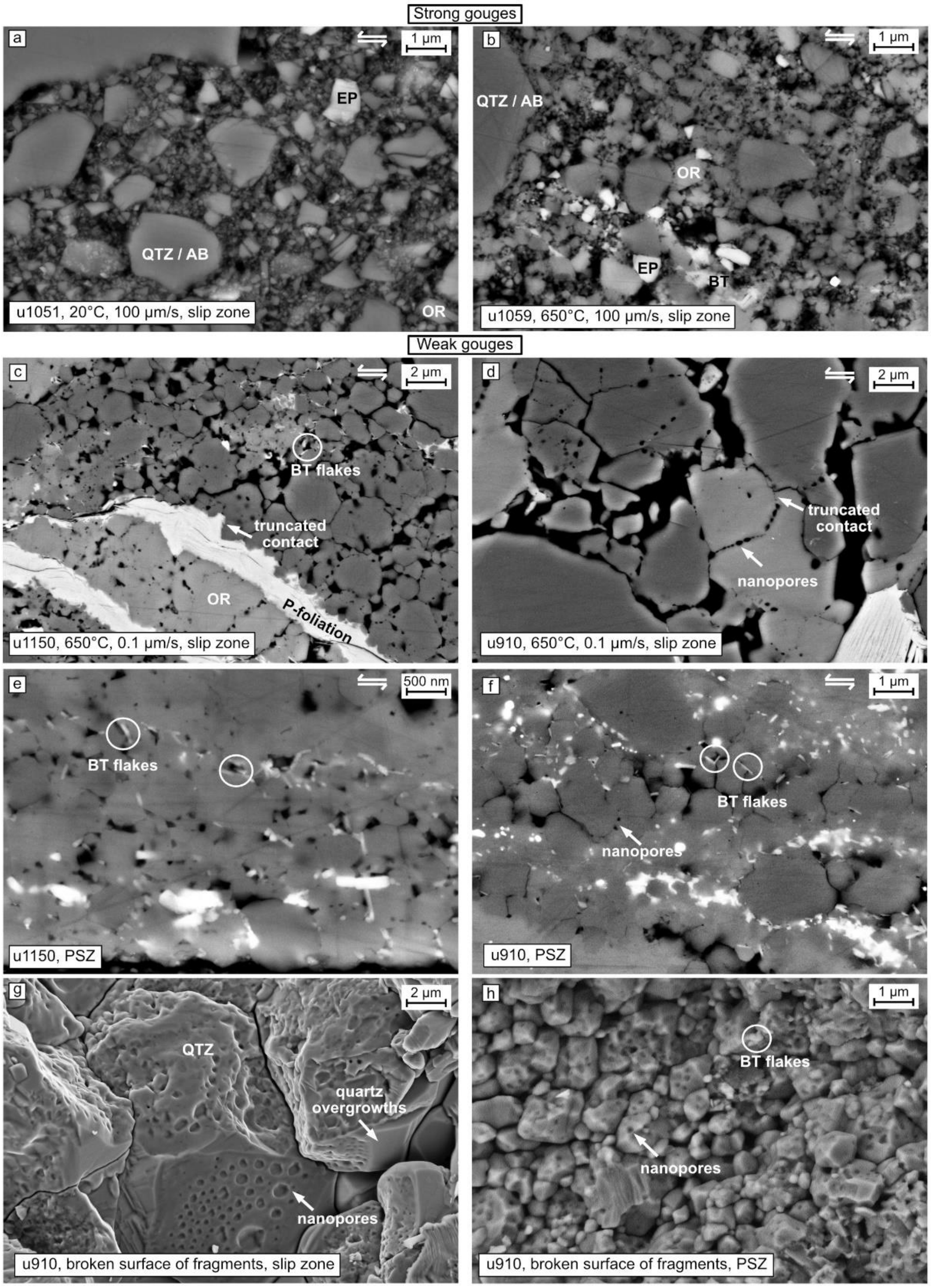


**Figure 5.** Backscatter images showing the variation in grain-scale microstructures between strong (a-b) and weak gouges (c-h). Three-dimensional views of nanopores and regional quartz overgrowths are displayed in (g-h). *QTZ / AB* quartz or albite; *OR* orthoclase; *EP* epidote; *BT* biotite.

## 4 Discussion

4.1. Frictional and viscous regimes

To compare our mechanical data with previous studies conducted at different effective normal stresses, we convert the steady-state shear stresses ($\tau_{ss}$) into apparent friction coefficients ($\mu_{ss}$) according to the formula below:

$$\mu_{ss} = \tau_{ss}/\sigma_n^{eff} \quad (2)$$

The effect of cohesion on friction coefficients is ignored, assuming this is negligible in powdered materials, in line with most previous works. The apparent friction coefficients obtained are shown against temperature in Figure 6, together with previously reported data. Table S2 summarizes the experimental conditions applied in the other studies and the range of measured friction coefficients. As shown in Figure 6, we classified the mechanical behavior of granitoid gouge in our study into two different regimes: the temperature-insensitive (frictional) regime and the temperature-sensitive (viscous) regime. This interpretation is consistent with the two regimes identified for westerly granite gouges (Blanpied et al., 1995), for pure quartz gouges (Chester & Higgs, 1992) and for calcite fault gouges (Verberne et al., 2015).

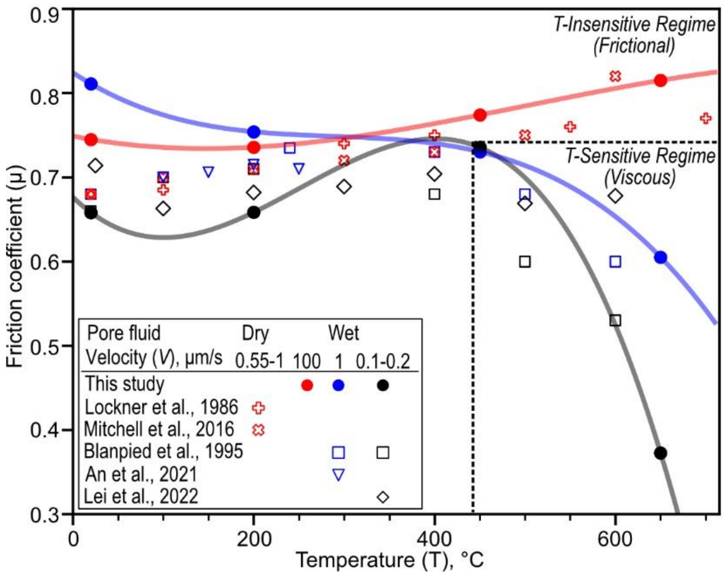


**Figure 6.** Comparison of steady-state friction coefficient for granitic gouges between our study and previous publications. Colorful shading and dashed lines are drawn as guides. Velocity refers to a range of displacement rates at which the friction coefficients were selected. See Table S1 for experimental conditions applied in the previous studies.

In the temperature-insensitive regime, the apparent friction coefficients $\mu_{ss}$ were generally high and relatively insensitive to temperature changes. In our study, this regime includes samples deformed at $V$ = 100 μm/s and $T$ = 20-650°C, and those deformed at $V$ = 0.1-1 μm/s and $T$ < 450°C. Many studies on granitoid gouges have reported similar friction coefficients (An et al., 2022; Blanpied et al., 1995; Kolawole et al., 2019; Lei et al., 2022a). It is important to note that these studies covered a broader range of effective normal stresses and pore fluid pressures in comparison to the conditions in our research (Table S2). This consistency in friction coefficients across varying effective normal stress and pore fluid pressure levels implies that the deformation mechanisms in this regime remain largely unaffected by such changes. Consequently, this suggests that the deformation processes are primarily frictional, similar to those observed in a wide range of frictionally deformed materials, ranging from metals to a variety of rock types (Rabinowicz & Mutis, 1965; Scholz, 2019).

In the temperature-sensitive regime, $\mu_{ss}$ showed a notable decrease as temperature increases. This regime includes samples deformed at $V$ = 0.1-1 μm/s and $T \geq$ 450 °C. This temperature-sensitive weakening behavior is most pronounced at a low sliding velocity of $V$ = 0.1 μm/s, where friction coefficients decreased from $\mu_{ss}$ = 0.74 at 450°C to $\mu_{ss}$ = 0.37 at 650°C, indicating also a rate-sensitivity in the viscous response. In addition, gouges sheared under high pore fluid pressure showed a more pronounced weakening effect compared to those with lower pore fluid pressure. For example, in our study, the apparent friction coefficients of gouges sheared at $V$ = 0.1 μm/s and $P_f$ = 100 MPa decreased by $\Delta\mu_{ss}$ = 0.37 from 450 °C to 650°C. In contrast, experiments by Lei et al., 2022a showed that granitoid gouges sheared at $V$ = 0.2 μm/s and $P_f$ = 30 MPa decreased by $\Delta\mu_{ss}$ = 0.03 from 400°C to 600°C (Figure 6). This temperature-, rate- and pore pressure-sensitivity suggests that fluid-assisted viscous processes predominantly govern deformation in this temperature-sensitive regime.

In our study of granitoid gouges, the principal weakening effect is induced by lowering the sliding velocity from $V$ = 100 μm/s to $V$ = 0.1 or 1 μm/s and by increasing the temperature from $T$ = 20°C to at least $T \approx$ 400-450°C (Figure 2d). The study of Blanpied et al., 1995 has shown that at low velocities of $V \approx$ 1 μm/s, the addition of pore fluids to dried gouges significantly reduced the friction coefficients through fluid-assisted processes, from $\mu_{ss} = 0.80$ to $\mu_{ss} = 0.58$ at 600°C. However, we observed that granitoid gouges subjected to wet ($P_f$ = 100 MPa) and fast shearing ($V$ = 100 μm/s) showed high friction coefficients $\mu_{ss} =$ 0.74-0.82, similar to $\mu_{ss} =$ 0.68-0.82 for gouges deformed at dry and low velocity conditions by Lockner & Byerlee, 1986 and Mitchell et al., 2016 (where $P_f$ = 0 MPa, $V$ = 0.55-1 μm/s). Our experiments reveal that only the addition of pore fluids does not necessarily weaken the gouge tested, but that fully water-saturated gouges with high pore fluid pressure can maintain their 'dry' frictional strength when sheared at a high enough velocity. This may be attributed to the dominance of frictional processes over time-dependent fluid-assisted processes at sufficiently rapid shearing rates, where dissolution/precipitation kinetics are too slow to play any role.

### 4.2. Deformation mechanisms

We use the schematic diagram in Figure 7 to comprehensively summarize the microstructural evolution of our granitoid gouges from the frictional to the viscous regime as a function of temperature and velocity. This diagram includes the microstructural changes at the gouge scale, as well as those at the grain scale, and provides a basis for discussing the operative deformation mechanisms. As shown in Figure 7b, the unsheared starting material is characterized by coarse clasts and large porosity, without any indication of strain localization. At low temperature or high velocity in the frictional regime, deformation is localized in a thick slip zone (> 149 μm, $\bar{d} \approx 5$ μm) close to the sample-piston interface (Figure 7c). The slip zones show clast-dominant texture, medium porosity and numerous fracture arrays. As temperature increases and velocity decreases during the transitional regime, gouges exhibit a higher degree of strain localization, resulting in a thin principal slip zone (PSZ) with mean grain size $\bar{d} < 1$ μm forming adjacent to the broader, less localized slip zone (Figure 7d). The PSZs show an ultrafine-grained and matrix-dominant texture with tiny biotite flakes filling grain-grain boundaries, while the broader slip zones retain their clast-dominant texture but with fewer fracture arrays and more closely spaced P-foliations. At the highest temperature and lowest velocity in the viscous regime, deformation localizes even further into a still thin PSZ (Figure 7e), whereas the slip zone shows a much smaller amount of fine-grained matrix, less fractures arrays, but extensive boundary-subparallel P-foliations and nanopores at grain contact surfaces.

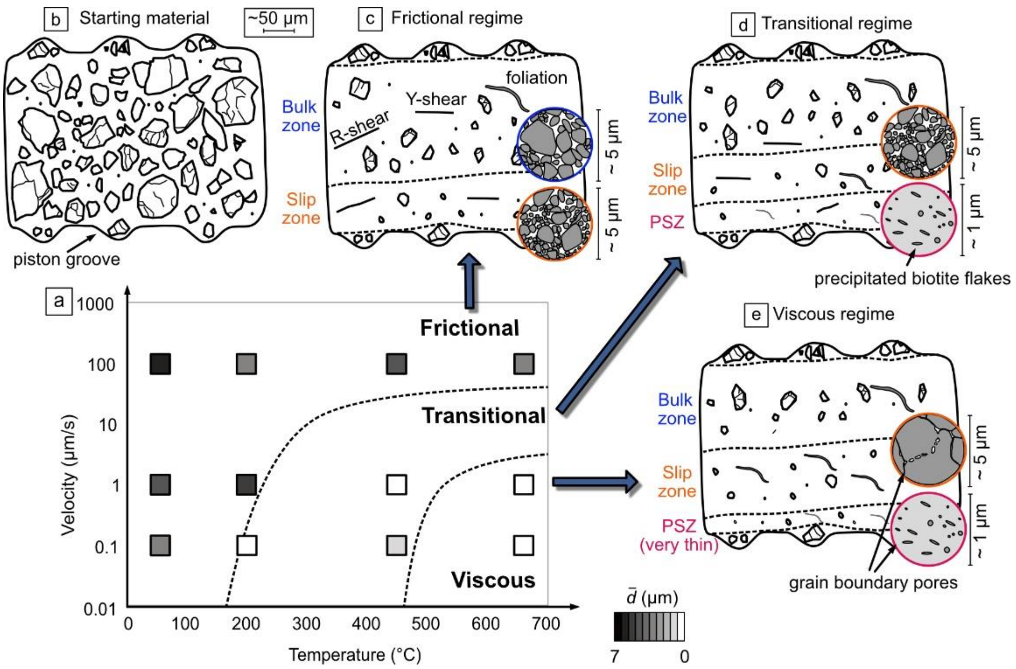


**Figure 7.** Schematic diagram summarizes the microstructural evolution from the frictional regime to the viscous regime as temperature increases, velocity decreases or grain size decreases. $\bar{d}$ is the mean diameter of particles within the (principal) slip zone (see detailed data in Table S1).

4.2.1. Deformation mechanism in the frictional regime

Microstructural evidence indicates that the temperature-insensitive deformation mechanism governing granitoid gouge deformation in the frictional regime is cataclastic frictional granular flow. In this regime, our deformed gouges underwent substantial particle fragmentation, resulting in significant grain size reduction relative to the starting material (Figure 7b-7c). Angular grain boundaries, as shown in Figure 5b, suggest a process of grain crushing and fracturing, rather than the typical interlocking and discrete grain boundaries found in viscous processes like DPC (Kilian et al., 2011; Marti et al., 2017). Pervasive fracture arrays crosscut the entire gouge layers (Figure 4a), which is characteristic of frictionally deformed fault rocks from many experiments (An et al., 2022; Blanpied et al., 1995; Logan et al., 1992) and natural fault zones (Frederick M. Chester et al., 1993; Faulkner et al., 2010; Wehrens et al., 2016). Furthermore, deformation typically localized into slip zones near the sample-piston interface, adjacent to a bulk zone in the center (Figure 4a, 4d). Both slip and bulk zone underwent frictional deformation, indicated by the similar clast-dominant gouge texture found within these areas (see Figure 5a-5b). The slip zones accommodate more deformation than the bulk zones, owing to their smaller clast size, larger volume of fine-grained matrix, and foliations oriented more parallel to the shear planes

(Figure 4a). These microstructural observations indicate that materials adjacent to the interface must have experienced a faster rate of deformation and correspondingly more intense frictional deformation, compared to the central region. The observed high strength is primarily determined by the actively deformed slip zones, where frictional resistance is caused by grain rotations, localized sliding along angular grain boundaries and on fracture arrays, i.e. by cataclastic frictional granular flow.

#### 4.2.2. Deformation mechanisms in the viscous regime

Regarding gouges from the viscous regime, microstructural evidence points to the simultaneous operation of DPC and cataclastic frictional granular flow. Specifically, gouges within this regime exhibited few fracture arrays, more regular P-foliations defined by well-aligned biotite and sigmoidal aggregates of fragmented orthoclase (Figure 4f). In nature, such features are typical for viscously deformed mylonites that form at elevated temperature/pressure conditions at depth (Passchier & Trouw, 1996; Smith et al., 2007; Viegas et al., 2014). By analogy to previous studies (Barker et al., 1991; Spiers et al., 1990), we infer for our experiments that the truncated and tight grain contacts indicate that dissolution has occurred at these sites because of stress concentration (Figure 5c-5d). Dissolved material is then transported and precipitated in dilatant, pore-rich domains under reduced stress, as exemplified by the formation of overgrowths on existing grain surfaces (quartz overgrowth in Figure 5g), or as precipitation along grain contacts (biotite flakes in Figure 5e-5f). The newly grown biotite flakes are not only extremely small in size and idiomorphic in shape, but also spatially clearly separated from the preexisting larger biotite grains. These microstructural features suggest that the new grain formation involves a crucial process of fluid-assisted mass transport exceeding the grain scale, which exclusively occurs during DPC rather than dynamic recrystallization (Herwegh & Jenni, 2001; Lu & He, 2018; Schwichtenberg et al., 2022).

Additionally, many nanopores were located mostly along the grain contact surfaces (Figure 5g), or within grains as fluid inclusions (Figure 5c-5d). These nanopores may either have been trapped within crystals during rapid overgrowths (Craw & Norris, 1993), or formed during preferential dissolution of crystallographic faces resulting in etch pits (Billia et al., 2013). Another process worth considering in the context of pore formation/preservation is creep cavitation during viscous grain boundary sliding (Fusseis et al., 2009; Gilgannon et al., 2017, 2020; Kassner & Hayes, 2003; Ree, 1994), which might contribute to the nucleation of these nanopores in the ultrafine-grained and dense domain (Figure 5h). While it remains challenging to determine which of these mechanisms primarily governs the formation of nanopores, the associated microstructures highlight the notably enhanced effect of viscous processes relative to the frictional ones within this regime. The formation of potentially interconnected dilatant openings provides the path for mass transportation, and creates space for dissolved material to precipitate and develop.

The observed strength reduction in the viscous regime is closely associated with the formation of the ultrafine-grained PSZ supporting a major role of a grain size sensitive creep mechanism, namely DPC. DPC operates by facilitating small displacements between intervening clasts through dissolving materials at the grain-to-grain contacts and then transporting to regions with lower stress concentration (Bart Bos & Spiers, 2002; Niemeijer, 2018). Unlike the cataclastic frictional granular flow, the rate of DPC strongly increases with decreasing grain size. This could be due to either a faster dissolution process, caused by a higher reactive surface area (Anbeek, 1992), or quicker diffusive transport process due to shorter transport distances at the grain scale (de Meer & Spiers, 1997; Xiangmin Zhang et al., 2010). We infer that the extremely small grain size within the PSZs allows DPC to operate at rates that are sufficiently rapid to accommodate the majority of sliding, and ultimately resulting in a reduction in the gouge strength. Moreover, the development of biotite foliations may also contributes to the reduction of gouge strength, e.g. through dislocation glide on the basal plane (Lu & He, 2014; Okamoto et al., 2019; Shea & Kronenberg, 1992), or through frictional slip on atomically flat basal planes (Aslin et al., 2019). Biotite, as a type of sheet silicate, generally exhibits a higher frictional strength if deformation involves buckling, bending or cleavage of grains (Niemeijer, 2018; Okamoto et al., 2019). Our microstructures reveal that both primary and newly precipitated biotite flakes in PSZs are small enough to inhibit buckling or further bending, thus reducing the apparent gouge strength (Figure 5e-5f, supporting information Figure S4).

To understand the process of formation of the ultrafine-grained PSZ, we repeated the experiment conducted at 650°C and 0.1 μm/s but terminated it at displacements of ~2 mm and ~5 mm. The sample sheared for ~2 mm displacement exhibited homogeneous deformation similar to the starting material, with no indication of a PSZ. However, we observed that some particles underwent substantial grain size reduction close to the boundary (Figure 8a). Subsequent shearing for a larger displacement of ~5 mm resulted in the development of a PSZ adjacent to the slip zone, characterized by microstructural features that we have associated with viscous behavior involving DPC (Figure 8b-8c). This observation suggests that a sufficient amount of displacement is necessary for frictional processes to reduce the grain size before activating grain-size-sensitive DPC within the PSZ. Once DPC is initiated, under considerably high temperature and slow velocity, the grain size may continue to decrease, through (subordinate) frictional processes or through dissolution and precipitation, resulting in additional strain localization or condensation of PSZ until a steady state condition is achieved.

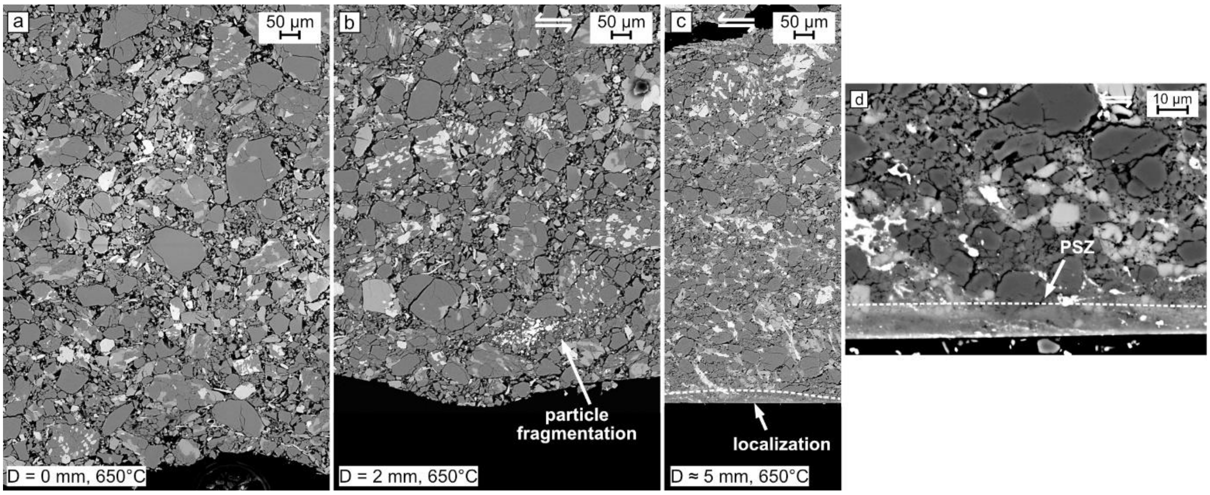


**Figure 8.** Mosaics of backscatter images of the gouge layers sheared at $T$ = 650°C, $V$ = 0.1 μm/s for (a) displacement of D = 0 mm, (b) D = 2 mm and (c) D ≈ 5 mm. The effective normal stresses were 100 MPa, 80 MPa and 150 MPa, respectively. (d) The close-up view of strain localized area in (c).

4.3. Rheology in the gradual transition from frictional to viscous regimes

In geologic materials and metallurgy, a standard power law is commonly used to characterize viscous or creep deformation, describing the dependency of strain rate on various factors such as differential stress, grain size and temperature. Such a constitutive flow law is generally expressed in the following general form (Gleason & Tullis, 1995; Twiss & Moores, 1992):

$$\dot{\varepsilon} = A\sigma^n d^{-m} f_{H_2O}^r \exp\left(-\frac{Q}{RT_K}\right) \quad (3)$$

Here, $\dot{\varepsilon}$ represents axial or equivalent strain rate, $A$ is the pre-exponantial factor, $\sigma^n$ is differential or deviatoric stress with exponent $n$, $d^{-m}$ is the grain size with exponent $m$, $f_{H_2O}^r$ is water fugacity with exponent $r$, $Q$ is the activation energy, $R$ is the gas constant, and $T_K$ is temperature in Kelvin. Generally, rock flow strength shows a linear or non-linear relationship with strain rate in a viscously deforming system, with stress exponents (stress sensitivity of strain rate) ranging from $n$ = 1 to $n$ = 4 or 5 (Luan & Paterson, 1992; Rutter & Brodie, 2004a, 2004b). The specific $n$ value serves as an indicator of the active creep mechanisms, such as dislocation creep ($n$ = 3 to 5; Weertman, 1978) and DPC ($n$ = 1; Spiers et al., 1990). In contrast, in a system undergoing purely frictional deformation, strain rate is extremely sensitive to stress ($n$ >> 5), or conversely strength is only very weakly dependent on strain rate (e.g. Chen et al., 2017).

To investigate in our experiments how temperature affects the transition from cataclastic frictional granular flow (high $n$) to DPC (low $n$), we calculate the stress exponent $n$ using the following formulas:

$$n = {\partial Ln\dot{\varepsilon}}/{\partial Ln\sigma} \quad (4a)$$

$$\dot{\varepsilon} = {\dot{\gamma}}/{\sqrt{3}} = {V}/{\sqrt{3}W} \quad (4b)$$

$$\sigma = \sqrt{3}\tau_{ss} \quad (4c)$$

In these formulas, $\dot{\gamma}$ represents the shear strain rate, $V$ is the applied sliding velocity, $\tau_{ss}$ is the shear stress obtained in our study, $W$ is the width of localized domains. The (equivalent) differential stress ($\sigma$) and (equivalent) strain rate ($\dot{\varepsilon}$) are calculated following the method described by Verberne et al., 2017. Due to varying degrees of strain localization, we consider $W$ to be the width of slip zones measured in the experiments conducted at 20-450°C and the width of the PSZs developed at 650°C (see detailed data in Table S3). In a log-log plot, the resulting (equivalent) strain rates are plotted against (equivalent) differential stresses for different temperatures ($T$ = 20, 200, 450, 650°C) (Figure 9). The slope ($n$) of the linear fits is determined exclusively at temperatures of 20°C and 650°C, as these temperatures provide enough data points to constrain the linear fits. Since quartz is generally considered to represent the dominant weak phase in viscously deforming granitoid systems (Bürgmann & Dresen, 2008; Kohlstedt et al., 1995), we also add the stress exponents obtained in quartz deformation experiments as reported in literature.

As illustrated in Figure 9, though constrained by very few data, the $n$ value for granitoid gouges decreases as the temperature increases: from $n \geq 17$ at 20-450°C to $n \approx 2$ at 650°C. The high $n$ values at low temperatures indicates that rock strength is almost independent of strain rate, and cataclastic frictional granular flow governs the deformation. At high temperature of 650°C, the low $n$ value obtained for granitoid gouges closely aligns with $n$ = 1.7 for a mix of dislocation and diffusion creep in quartz (Fukuda et al., 2018), and is close to $n$ = 1 expected if DPC or DPC-accommodated granular flow becomes dominant.

However, dislocation creep cannot account as a dominant mechanism in the case of our fine-grained polymineralic gouge aggregates due to the pinning effect of secondary phases (Kilian et al., 2011; Passchier & Trouw, 1996). Hence, the changes in *n*-values in Figure 9 suggest that the contributions of the end-member mechanisms change with temperature, from velocity-strengthening cataclastic frictional granular flow (Chen et al., 2017; Chen & Spiers, 2016) to DPC-accommodated viscous granular flow becoming dominant, as temperatures exceed 450°C and as strain localizes into the ultra-fine grained PSZs.

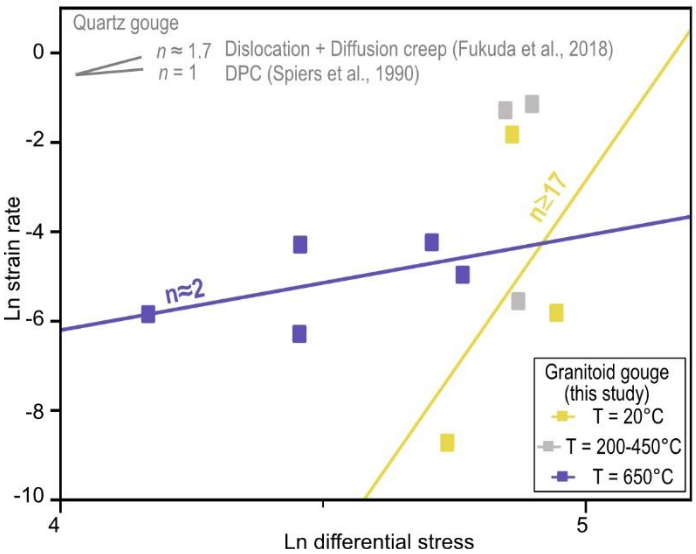


**Figure 9.** Ln strain rate vs. Ln differential stress showing the effect of temperature on the stress exponent (*n*). Stress exponents of quartz gouges represent different creep mechanisms: $n \approx 1.7$ for a mixed dislocation and diffusion creep in quartz (Fukuda et al., 2018); $n = 1$ predicted by conventional models for DPC (Spiers et al., 1990).

### 4.4. Implications for natural fault zones

It is important to note that our experimental findings can only be extrapolated to natural granitoid gouges under water saturated conditions and not for dry gouges. In Figure 10, we extend the experimental strength data obtained in our experimental study to conditions representative of natural fault zones. This extension is established based on the following assumptions: (1) the strength refers to the differential stress needed for the initiation of sliding along a pre-existing fault plane under strike-slip kinematic conditions; (2) existence of a geothermal gradient of 25°C/km (e.g. estimates from the Aar Massif by Berger & Herwegh, 2019; Musso Piantelli, 2023); (3) existence of a lithostatic pressure gradient of 27.5 MPa/km, following Blanpied et al., (1995). We examined two cases: the first case assumes an interconnected porosity and therefore the pore fluid pressure is hydrostatic ($\lambda$ = pore fluid pressure/lithostatic pressure = 0.4); in the second case, substantial amounts of water are trapped and therefore isolated in pores meaning that the fluid pore pressure is close to the lithostatic pressure (λ = 0.9, close to a value of 1). Note that if we allow the state of stress to vary along changes in the kinematic framework (e.g. normal or thrust faulting), the amplitude of the strength envelope simply scales up/down, while the depth of the frictional-viscous transition remains relatively unaffected. Here, we focus on the strength envelope constructed based on aforementioned assumptions only.

For the hydrostatic and near-lithostatic fluid pressure conditions, the experimental (apparent) friction coefficients are extrapolated in the following way: first, the presumed geothermal gradient is used to extrapolate the experiment temperatures to the corresponding crustal depths. Then, the effective normal stress involves subtracting the pore fluid pressure from the normal stress expected at each depth (Figure 10a). The normal stress is obtained by multiplying the lithostatic pressure gradient with the depth calculated at the corresponding temperature, while the expected pore fluid pressure is determined as λ times the normal stress. Finally, the calculation of strengths involves multiplying the effective normal stress with the apparent friction coefficients ($\mu_{ss}$) of those experiments sheared at a strain rate of $10^{-3}$ $s^{-1}$ to $10^{-4}$ $s^{-1}$ (sliding velocity $V = 0.1$ μm/s), as reported in Table 1, and converting them to differential stresses (strength) using formula (4c). The strength envelope is a curved best-fit line to the data points extrapolated from our experiments up to a temperature of ~650°C, which corresponds to a depth of 26 km.

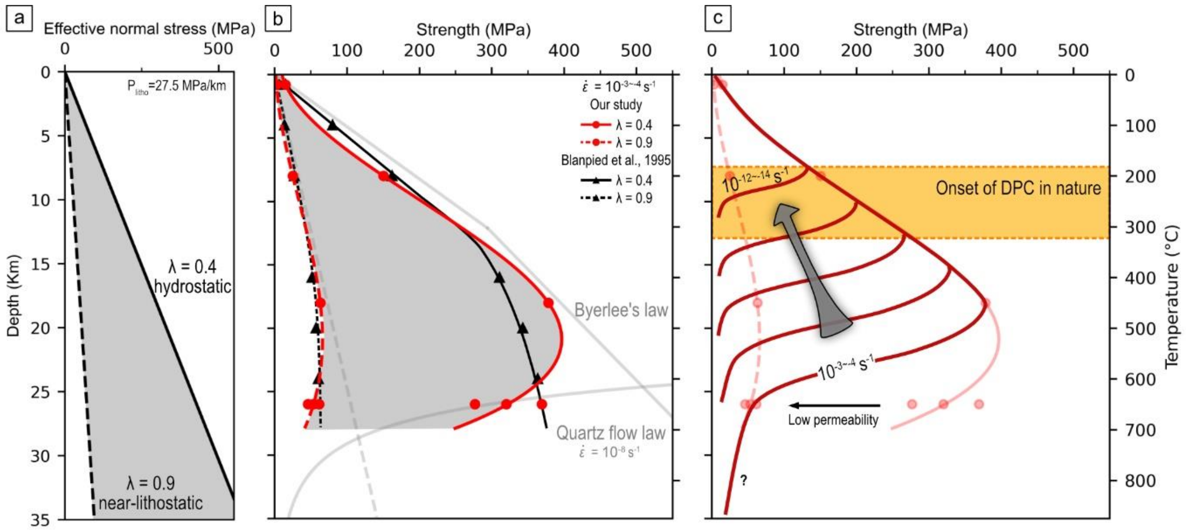


**Figure 10.** Extrapolation of experimental data for wet granitoid gouge to natural fault zones. The geothermal gradient is 25°C/km. In (a), the effective normal stress against depth assumed in two types of extrapolations: the hydrostatic pressure condition (λ = 0.4), and the near-lithostatic fluid pressure condition (λ = 0.9). (b) Plot of strength against depth, with

references to extrapolation of westerly granite gouges (Blanpied et al., 1995, recalculated according to the assumptions in this study), Byerlee's law (J. Byerlee, 1978) and the quartz flow law (Fukuda et al., 2018). $\dot{\boldsymbol{\varepsilon}}$ = (equivalent) strain rate. The curved strength envelope is the best-fit line to the data points. (c) Conceptually extrapolated strength to slow strain rates of $10^{-12\sim-14}$ $s^{-1}$ typical in natural fault zones. Yellow rectangle indicates the onset temperature of dissolution-precipitation creep in nature.

Our extrapolation in Figure 10b shows that the predicted strengths are generally much lower in the case of near-lithostatic fluid pressures, with a peak value of ~60 MPa, compared to a peak value of ~360 MPa in the hydrostatic pressure conditions. For both cases, the calculated strengths of granitoid gouges increase nearly linearly with depth, down up to ~18 km, which aligns well with the previous extrapolation of sheared granitic gouges from Blanpied et al., 1995 and Byerlee's law. However, a significant deviation occurs at greater depths, where calculated strengths from our study show a substantial decrease at a depth of >20 km, particularly in the hydrostatic conditions. This difference in extrapolated strengths may be attributed to variations in the total displacement applied in these two studies. In our study, gouges that underwent displacement-weakening reached a (near) steady state low strength after sliding for a minimum of ~3 mm displacement (Figure 2c). In contrast, Blanpied et al.'s 1995 study sheared gouges at a similar slow strain rate but only for <1 mm displacement, preventing steady state to be reached. Our results emphasis the importance of not only relatively high temperature and slow strain rates, but also of sufficient displacement for grain size reduction to activate DPC and to activate further weakening (see section 4.2.2).

These findings from our study have important consequences for the extrapolation of our experimental results to natural conditions with commonly much slower strain rates (except for seismic and slow slip cycles), and much lower permeability at middle-lower crustal levels predicted by crustal-scale models (Ingebritsen & Manning, 1999). Under low temperature and shallow crustal conditions, granitoid fault gouges are typically non-cohesive, porous and do not display substantial fault healing by cementation processes (exceptions are hydrothermally active fault zones, e.g. see Berger & Herwegh, 2019, 2022; Niwa et al., 2016). In this case, pores are interconnected, therefore the pore fluid pressure is hydrostatic. Under high temperature and deeper crustal conditions, elevated pore fluids successively form because fluids become trapped along grain boundary pores or along transgranular cracks and cementation (fault healing; Tenthorey et al., 2003). Consequently, interconnectivity of pore spaces decreases and so does the permeability. In our case, the near-lithostatic pressure condition is valid for natural gouges at the same rates as in the experiments at T ≥ 450°C. This is consistent with abundant nanopore inclusions formed within dense PSZs due to DPC-accommodated viscous granular flow (see section 3.2.3). With these considerations, as shown in Figure 10c, the strength envelope of natural fault zones are a combination of two end member cases studied: a hydrostatic case at T < 450°C and a near-lithostatic fluid pressure case in the range of T = 450°C-650°C.

Furthermore, the laboratory observed DPC-induced weakening effect is expected to occur at all P/T conditions where natural records of synkinematic dissolution-precipitation processes are found in granitoid gouges. Newly precipitated mica (Berger et al., 2017), stylolites (Groshong, Jr., 1988) and fluid inclusions (Harrison & Onasch, 2000) in granitoid rocks were found in the temperature range of 180°C-320°C, which corresponds to anchizonal, in combination with the variations in sliding velocities and grain sizes under natural deformation conditions, are important parameters which can explain the wide depth range (7-20 km) of the viscous-frictional transition inferred for the granitoid continental crust.

## 5 Conclusions

We performed sliding experiments on granitoid gouges at a broad range of sliding velocities (*V* = 0.1, 1, 100 μm/s) and temperatures (*T* = 20, 200, 450, 650°C), over a large displacement of ~15 mm, and at an effective normal stress and pore fluid pressure of 100 MPa, respectively. Microstructures of compacted-only and sheared samples were quantitatively analyzed. The following conclusions can be drawn:

1. The strength of granitoid gouge was reduced from $\tau_{ss} \approx 75$ MPa at $T = 20$°C and $V = 100$ μm/s, to $\tau_{ss} \approx 37$ MPa at $T = 650$°C and $V = 0.1$ μm/s.

2. As the gouge weakened, strain localized into an ultrafine-grained and dense principal slip zone (PSZ), where nanopores were located along grain contact surfaces and contained biotite-quartz-feldspar precipitates. This evolution in microstructures indicates a transition in deformation mechanisms from cataclastic frictional granular flow to dissolution-precipitation creep (DPC) accommodated viscous granular flow.

3. The frictional-viscous transition occurred at $T \geq 450$°C, $V \leq 1$ μm/s, and/or for a median grain size < ~1 μm under the hydrothermal conditions tested in our study.

4. Prior to the formation of a PSZ and associated gouge weakening, gouges sheared at a short displacement of ~2 μm underwent substantial grain size reduction close to the sample boundary, suggesting that a sufficient additional displacement is necessary (i.e. a displacement and grain size threshold must be overcome) to activate DPC.

6. Though poorly constrained by only limited data, the average stress exponent (*n*) at the deformation temperature of 20-450°C was ≥17, and at 650°C was ~2, suggesting an increased contribution of DPC at high temperature.

7. Extrapolations of experimental data to construct crustal strength suggest that the frictional-viscous transition may be triggered at temperatures of 180-320°C (or depth of 7-20 km depending on the geothermal gradient), at slow natural strain rates and in ultrafine-grained fault gouges, due to activation of DPC.

**Acknowledgments**

We thank Thony van der Gon Netscher, Gerard Kuijpers, and Floris van Oort for technical supports of the ring shear apparatus, Beatrice Frey for support in the FEG-SEM works, and Frank Emanuel Gfeller for support in the XRD works. This study is funded by the Swiss National Science Foundation (SNSF) grant number 192124.

## References

An, M., Zhang, F., Min, K., Elsworth, D., He, C., & Zhao, L. (2022). Frictional Stability of Metamorphic Epidote in Granitoid Faults Under Hydrothermal Conditions and Implications for Injection-Induced Seismicity. *Journal of Geophysical Research: Solid Earth*, *127*(3), e2021JB023136. https://doi.org/10.1029/2021JB023136

Anbeek, C. (1992). The dependence of dissolution rates on grain size for some fresh and weathered feldspars. *Geochimica et Cosmochimica Acta*, *56*(11), 3957–3970. https://doi.org/10.1016/0016-7037(92)90009-8

Aslin, J., Mariani, E., Dawson, K., & Barsoum, M. W. (2019). Ripplocations provide a new mechanism for the deformation of phyllosilicates in the lithosphere. *Nature Communications*, *10*(1), 686. https://doi.org/10.1038/s41467-019-08587-2

Barbarin, B. (1999). A review of the relationships between granitoid types, their origins and their geodynamic environments. *Lithos, 46*(3), 605–626. https://doi.org/10.1016/S0024-4937(98)00085-1

Barker, C. E., Burruss, R. C., Kopp, O. C., Machel, H. G., Marshall, D. J., Wright, P., & Colbum, H. Y. (1991). *Luminescence Microscopy and SpectroscopyQualitative and Quantitative Applications*. SEPM Society for Sedimentary Geology. https://doi.org/10.2110/scn.91.25

Baumberger, R., Herwegh, M., & Kissling, E. (2022). Remote Sensing and Field Data Based Structural 3D Modelling (Haslital, Switzerland) in Combination with Uncertainty Estimation and Verification by Underground Data. In *3D Digital Geological Models* (pp. 159–197). John Wiley & Sons, Ltd. https://doi.org/10.1002/9781119313922.ch10

Behnsen, J., & Faulkner, D. R. (2011). Water and argon permeability of phyllosilicate powders under medium to high pressure. *Journal of Geophysical Research: Solid Earth, 116*(B12). https://doi.org/10.1029/2011JB008600

Berger, A., & Herwegh, M. (2019). Cockade structures as a paleo-earthquake proxy in upper crustal hydrothermal systems. *Scientific Reports*, *9*(1), 9209. https://doi.org/10.1038/s41598-019-45488-2

Berger, A., & Herwegh, M. (2022). Grain-size-reducing- and mass-gaining processes in different hydrothermal fault rocks. *Geological Magazine*, *159*(11–12), 2219–2237. https://doi.org/10.1017/S0016756822000218

Berger, A., Herwegh, M., Schwarz, J.-O., & Putlitz, B. (2011). Quantitative analysis of crystal/grain sizes and their distributions in 2D and 3D. *Journal of Structural Geology, 33*(12), 1751–1763. https://doi.org/10.1016/j.jsg.2011.07.002

Berger, A., Wehrens, P., Lanari, P., Zwingmann, H., & Herwegh, M. (2017). Microstructures, mineral chemistry and geochronology of white micas along a retrograde evolution: An example from the Aar massif (Central Alps, Switzerland). *Tectonophysics*, *721*, 179–195. https://doi.org/10.1016/j.tecto.2017.09.019

Billia, M. A., Timms, N. E., Toy, V. G., Hart, R. D., & Prior, D. J. (2013). Grain boundary dissolution porosity in quartzofeldspathic ultramylonites: Implications for permeability enhancement and weakening of mid-crustal shear zones. *Journal of Structural Geology*, *53*, 2–14. https://doi.org/10.1016/j.jsg.2013.05.004

Blanpied, M. L., Lockner, D. A., & Byerlee, J. D. (1995). Frictional slip of granite at hydrothermal conditions. *Journal of Geophysical Research: Solid Earth*, *100*(B7), 13045–13064. https://doi.org/10.1029/95JB00862

Bos, B, & Spiers, C. J. (2001). Experimental investigation into the microstructural and mechanical evolution of phyllosilicate-bearing fault rock under conditions favouring pressure solution. *Journal of Structural Geology*, *23*(8), 1187–1202. https://doi.org/10.1016/S0191-8141(00)00184-X

Bos, Bart, & Spiers, C. J. (2002). Frictional-viscous flow of phyllosilicate-bearing fault rock: Microphysical model and implications for crustal strength profiles. *Journal of Geophysical Research: Solid Earth*, *107*(B2), ECV 1-1-ECV 1-13. https://doi.org/10.1029/2001JB000301

Bürgmann, R., & Dresen, G. (2008). Rheology of the Lower Crust and Upper Mantle: Evidence from Rock Mechanics, Geodesy, and Field Observations. *Annual Review of Earth and Planetary Sciences*, *36*(1), 531–567. https://doi.org/10.1146/annurev.earth.36.031207.124326

Burov, E. B. (2011). Rheology and strength of the lithosphere. *Marine and Petroleum Geology*, *28*(8), 1402–1443. https://doi.org/10.1016/j.marpetgeo.2011.05.008

Byerlee, J. (1978). Friction of Rocks. In J. D. Byerlee & M. Wyss (Eds.), *Rock Friction and Earthquake Prediction* (pp. 615–626). Basel: Birkhäuser. https://doi.org/10.1007/978-3-0348-7182-2_4

Chen, J., & Spiers, C. J. (2016). Rate and state frictional and healing behavior of carbonate fault gouge explained using microphysical model: Microphysical Model for Friction. *Journal of Geophysical Research: Solid Earth*, *121*(12), 8642–8665. https://doi.org/10.1002/2016JB013470

Chen, J., Niemeijer, A. R., & Spiers, C. J. (2017). Microphysically Derived Expressions for Rate-and-State Friction Parameters, $a$ , $b$ , and $D_c$ : Microphysically Derived RSF Parameters. *Journal of Geophysical Research: Solid Earth*, *122*(12), 9627–9657. https://doi.org/10.1002/2017JB014226

Chester, F. M., & Higgs, N. G. (1992). Multimechanism friction constitutive model for ultrafine quartz gouge at hypocentral conditions. *Journal of Geophysical Research: Solid Earth*, *97*(B2), 1859–1870. https://doi.org/10.1029/91JB02349

Chester, Frederick M., Evans, J. P., & Biegel, R. L. (1993). Internal structure and weakening mechanisms of the San Andreas Fault. *Journal of Geophysical Research: Solid Earth*, *98*(B1), 771–786. https://doi.org/10.1029/92JB01866

Craw, D., & Norris, R. J. (1993). Grain boundary migration of water and carbon dioxide during uplift of garnet-zone Alpine Schist, New Zealand. *Journal of Metamorphic Geology*, *11*(3), 371–378. https://doi.org/10.1111/j.1525-1314.1993.tb00154.x

Evans, B., Fredrich, J. T., & Wong, T.-F. (1990). The Brittle-Ductile Transition in Rocks: Recent Experimental and Theoretical Progress. In *The Brittle-Ductile Transition in Rocks* (pp. 1–20). American Geophysical Union (AGU). https://doi.org/10.1029/GM056p0001

Faulkner, D. R., Jackson, C. A. L., Lunn, R. J., Schlische, R. W., Shipton, Z. K., Wibberley, C. A. J., & Withjack, M. O. (2010). A review of recent developments concerning the structure, mechanics and fluid flow properties of fault zones. *Journal of Structural Geology*, *32*(11), 1557–1575. https://doi.org/10.1016/j.jsg.2010.06.009

Fukuda, J., Holyoke, C. W., & Kronenberg, A. K. (2018). Deformation of Fine-Grained Quartz Aggregates by Mixed Diffusion and Dislocation Creep. *Journal of Geophysical Research: Solid Earth*, *123*(6), 4676–4696. https://doi.org/10.1029/2017JB015133

Fusseis, F., Regenauer-Lieb, K., Liu, J., Hough, R. M., & De Carlo, F. (2009). Creep cavitation can establish a dynamic granular fluid pump in ductile shear zones. *Nature, 459*(7249), 974–977. https://doi.org/10.1038/nature08051

Giese, J., Seward, D., Stuart, F. M., Wüthrich, E., Gnos, E., Kurz, D., et al. (2010). Electrodynamic Disaggregation: Does it Affect Apatite Fission-Track and (U-Th)/He Analyses? *Geostandards and Geoanalytical Research*, *34*(1), 39–48. https://doi.org/10.1111/j.1751-908X.2009.00013.x

Gilgannon, J., Fusseis, F., Menegon, L., Regenauer-Lieb, K., & Buckman, J. (2017). Hierarchical creep cavity formation in an ultramylonite and implications for phase mixing. *Solid Earth*, *8*(6), 1193–1209. https://doi.org/10.5194/se-8-1193-2017

Gilgannon, J., Poulet, T., Berger, A., Barnhoorn, A., & Herwegh, M. (2020). Dynamic Recrystallization Can Produce Porosity in Shear Zones. *Geophysical Research Letters*, *47*(7), e2019GL086172. https://doi.org/10.1029/2019GL086172

Gleason, G. C., & Tullis, J. (1995). A flow law for dislocation creep of quartz aggregates determined with the molten salt cell. *Tectonophysics, 247*(1), 1–23. https://doi.org/10.1016/0040-1951(95)00011-B

Goetze, C., & Evans, B. (1979). Stress and temperature in the bending lithosphere as constrained by experimental rock mechanics. *Geophysical Journal International*, *59*(3), 463–478. https://doi.org/10.1111/j.1365-246X.1979.tb02567.x

Gratier, J.-P., Dysthe, D. K., & Renard, F. (2013). The Role of Pressure Solution Creep in the Ductility of the Earth's Upper Crust. In *Advances in Geophysics* (Vol. 54, pp. 47–179). Elsevier. https://doi.org/10.1016/B978-0-12-380940-7.00002-0

Gratier, J.-P., Menegon, L., & Renard, F. (2023). Pressure Solution Grain Boundary Sliding as a Large Strain Mechanism of Superplastic Flow in the Upper Crust. *Journal of Geophysical Research: Solid Earth*, *128*(4), e2022JB026019. https://doi.org/10.1029/2022JB026019

Griggs, D. (1967). Hydrolytic Weakening of Quartz and Other Silicates*. *Geophysical Journal of the Royal Astronomical Society*, *14*(1–4), 19–31. https://doi.org/10.1111/j.1365-246X.1967.tb06218.x

Groshong, Jr., R. H. (1988). Low-temperature deformation mechanisms and their interpretation. *Geological Society of America Bulletin*, *100*(9), 1329–1360. https://doi.org/10.1130/0016-7606(1988)100<1329:LTDMAT>2.3.CO;2

Harrison, M. J., & Onasch, C. M. (2000). Quantitative assessment of low-temperature deformation mechanisms in a folded quartz arenite, Valley and Ridge Province, West Virginia. *Tectonophysics*, *317*(1–2), 73–91. https://doi.org/10.1016/S0040-1951(99)00271-1

den Hartog, S. A. M., Niemeijer, A. R., & Spiers, C. J. (2012). New constraints on megathrust slip stability under subduction zone P–T conditions. *Earth and Planetary Science Letters*, *353–354*, 240–252. https://doi.org/10.1016/j.epsl.2012.08.022

Herwegh, M., & Jenni, A. (2001). Granular ¯ow in polymineralic rocks bearing sheet silicates: new evidence from natural examples.

Hickman, S., Sibson, R., & Bruhn, R. (1995). Introduction to Special Section: Mechanical Involvement of Fluids in Faulting. *Journal of Geophysical Research: Solid Earth*, *100*(B7), 12831–12840. https://doi.org/10.1029/95JB01121

Hirth, G., & Tullis, J. (1992). Dislocation creep regimes in quartz aggregates. *Journal of Structural Geology*, *14*(2), 145–159. https://doi.org/10.1016/0191-8141(92)90053-Y

Hirth, G., & Tullis, J. (1994). The brittle-plastic transition in experimentally deformed quartz aggregates. *Journal of Geophysical Research: Solid Earth*, *99*(B6), 11731–11747. https://doi.org/10.1029/93JB02873

Ingebritsen, S. E., & Manning, C. E. (1999). Geological implications of a permeability-depth curve for the continental crust. *Geology*, *27*(12), 1107. https://doi.org/10.1130/0091-7613(1999)027<1107:GIOAPD>2.3.CO;2

Johannes, W. (1984). Beginning of melting in the granite system Qz-Or-Ab-An-H2O. *Contributions to Mineralogy and Petrology*, *86*(3), 264–273. https://doi.org/10.1007/BF00373672

Kassner, M. E., & Hayes, T. A. (2003). Creep cavitation in metals. *International Journal of Plasticity*, *19*(10), 1715–1748. https://doi.org/10.1016/S0749-6419(02)00111-0

Kilian, R., Heilbronner, R., & Stünitz, H. (2011). Quartz grain size reduction in a granitoid rock and the transition from dislocation to diffusion creep. *Journal of Structural Geology*, *33*(8), 1265–1284. https://doi.org/10.1016/j.jsg.2011.05.004

Kirkpatrick, J. D., Fagereng, Å., & Shelly, D. R. (2021). Geological constraints on the mechanisms of slow earthquakes. *Nature Reviews Earth & Environment*, *2*(4), 285–301. https://doi.org/10.1038/s43017-021-00148-w

Kohlstedt, D. L., Evans, B., & Mackwell, S. J. (1995). Strength of the lithosphere: Constraints imposed by laboratory experiments. *Journal of Geophysical Research: Solid Earth*, *100*(B9), 17587–17602. https://doi.org/10.1029/95JB01460

Kolawole, F., Johnston, C. S., Morgan, C. B., Chang, J. C., Marfurt, K. J., Lockner, D. A., et al. (2019). The susceptibility of Oklahoma's basement to seismic reactivation. *Nature Geoscience*, *12*(10), 839–844. https://doi.org/10.1038/s41561-019-0440-5

Labuz, J. F., & Zang, A. (2012). Mohr–Coulomb Failure Criterion. *Rock Mechanics and Rock Engineering*, *45*(6), 975–979. https://doi.org/10.1007/s00603-012-0281-7

Lamadrid, H. M., Lamb, W. M., Santosh, M., & Bodnar, R. J. (2014). Raman spectroscopic characterization of H2O in CO2-rich fluid inclusions in granulite facies metamorphic rocks. *Gondwana Research*, *26*(1), 301–310. https://doi.org/10.1016/j.gr.2013.07.003

Lei, H., Zhou, Y., Yao, W., Ma, X., He, C., Dang, J., et al. (2022). Earthquake nucleation conditions of Anninghe Fault constrains from frictional experiments on natural granite gouge. *Chinese Journal of Geophysics*, *65*(3), 978–991. https://doi.org/10.6038/cjg2022P0248

Lei, H., Niemeijer, A. R., Zhou, Y., & Spiers, C. J. (2022). *Seismic potential of the Anninghe Fault zone, southeastern Tibetan Plateau: Constrains from friction experiments on natural granite gouge* (No. EGU22-6560). Presented at the EGU22, Copernicus Meetings. https://doi.org/10.5194/egusphere-egu22-6560

Lockner, D. A., & Byerlee, J. D. (1986). *Open File Report* (Open-File Report).

Logan, J. M., Dengo, C. A., Higgs, N. G., & Wang, Z. Z. (1992). Chapter 2 Fabrics of Experimental Fault Zones: Their Development and Relationship to Mechanical Behavior. In *International Geophysics* (Vol. 51, pp. 33–67). Elsevier. https://doi.org/10.1016/S0074-6142(08)62814-4

Lu, Z., & He, C. (2014). Frictional behavior of simulated biotite fault gouge under hydrothermal conditions. *Tectonophysics*, *622*, 62–80. https://doi.org/10.1016/j.tecto.2014.03.002

Lu, Z., & He, C. (2018). Friction of foliated fault gouge with a biotite interlayer at hydrothermal conditions. *Tectonophysics*, *740–741*, 72–92. https://doi.org/10.1016/j.tecto.2018.05.003

Luan, F. C., & Paterson, M. S. (1992). Preparation and deformation of synthetic aggregates of quartz. *Journal of Geophysical Research: Solid Earth*, *97*(B1), 301–320. https://doi.org/10.1029/91JB01748

Marti, S., Stünitz, H., Heilbronner, R., Plümper, O., & Drury, M. (2017). Experimental investigation of the brittle-viscous transition in mafic rocks – Interplay between fracturing, reaction, and viscous deformation. *Journal of Structural Geology*, *105*, 62–79. https://doi.org/10.1016/j.jsg.2017.10.011

de Meer, S., & Spiers, C. J. (1997). Uniaxial compaction creep of wet gypsum aggregates. *Journal of Geophysical Research: Solid Earth*, *102*(B1), 875–891. https://doi.org/10.1029/96JB02481

Mitchell, E. K., Fialko, Y., & Brown, K. M. (2016). Velocity-weakening behavior of Westerly granite at temperature up to 600°C. *Journal of Geophysical Research: Solid Earth*, *121*(9), 6932–6946. https://doi.org/10.1002/2016JB013081

Nakatani, M., & Scholz, C. H. (2004). Frictional healing of quartz gouge under hydrothermal conditions: 1. Experimental evidence for solution transfer healing mechanism. *Journal of Geophysical Research: Solid Earth*, *109*(B7). https://doi.org/10.1029/2001JB001522

Niemeijer, A. R. (2018). Velocity-dependent slip weakening by the combined operation of pressure solution and foliation development. *Scientific Reports*, *8*(1), 4724. https://doi.org/10.1038/s41598-018-22889-3

Niemeijer, A. R., Spiers, C. J., & Bos, B. (2002). Compaction creep of quartz sand at 400–600°C: experimental evidence for dissolution-controlled pressure solution. *Earth and*

*Planetary Science Letters*, *195*(3–4), 261–275. https://doi.org/10.1016/S0012-821X(01)00593-3

Niemeijer, A. R., Spiers, C. J., & Peach, C. J. (2008). Frictional behaviour of simulated quartz fault gouges under hydrothermal conditions: Results from ultra-high strain rotary shear experiments. *Tectonophysics*, *460*(1–4), 288–303. https://doi.org/10.1016/j.tecto.2008.09.003

Niwa, M., Shimada, K., Aoki, K., & Ishimaru, T. (2016). Microscopic features of quartz and clay particles from fault gouges and infilled fractures in granite: Discriminating between active and inactive faulting. *Engineering Geology*, *210*, 180–196. https://doi.org/10.1016/j.enggeo.2016.06.013

Okamoto, A. S., Verberne, B. A., Niemeijer, A. R., Takahashi, M., Shimizu, I., Ueda, T., & Spiers, C. J. (2019). Frictional Properties of Simulated Chlorite Gouge at Hydrothermal Conditions: Implications for Subduction Megathrusts. *Journal of Geophysical Research: Solid Earth*, *124*(5), 4545–4565. https://doi.org/10.1029/2018JB017205

Okuda, H., Niemeijer, A. R., Takahashi, M., Yamaguchi, A., & Spiers, C. J. (2023). Hydrothermal Friction Experiments on Simulated Basaltic Fault Gouge and Implications for Megathrust Earthquakes. *Journal of Geophysical Research: Solid Earth*, *128*(1), e2022JB025072. https://doi.org/10.1029/2022JB025072

Passchier, C., & Trouw, R. A. (1996). *Microtectonics*. *Microtectonics*. https://doi.org/10.1007/3-540-29359-0

Paterson, M. S., & Wong, T. (2005). *Experimental rock deformation--the brittle field* (2nd, completely rev. and updated ed ed.). Berlin ; New York: Springer.

Rabinowicz, E., & Mutis, A. (1965). Effect of abrasive particle size on wear. *Wear*, *8*(5), 381–390. https://doi.org/10.1016/0043-1648(65)90169-9

Ree, J.-H. (1994). Grain boundary sliding and development of grain boundary openings in experimentally deformed octachloropropane. *Journal of Structural Geology*, *16*(3), 403–418. https://doi.org/10.1016/0191-8141(94)90044-2

Rutter, E. H. (1983). Pressure solution in nature, theory and experiment. *Journal of the Geological Society*, *140*(5), 725–740. https://doi.org/10.1144/gsjgs.140.5.0725

Rutter, E. H., & Brodie, K. H. (2004a). Experimental grain size-sensitive flow of hot-pressed Brazilian quartz aggregates. *Journal of Structural Geology*, *26*(11), 2011–2023. https://doi.org/10.1016/j.jsg.2004.04.006

Rutter, E. H., & Brodie, K. H. (2004b). Experimental intracrystalline plastic flow in hot-pressed synthetic quartzite prepared from Brazilian quartz crystals. *Journal of Structural Geology*, *26*(2), 259–270. https://doi.org/10.1016/S0191-8141(03)00096-8

Rybacki, E., & Dresen, G. (2004). Deformation mechanism maps for feldspar rocks. *Tectonophysics*, *382*(3–4), 173–187. https://doi.org/10.1016/j.tecto.2004.01.006

Sammis, C., King, G., & Biegel, R. (1987). The kinematics of gouge deformation. *Pure and Applied Geophysics*, *125*(5), 777–812. https://doi.org/10.1007/BF00878033

Schneeberger, R., Mäder, U. K., & Waber, H. N. (2017). Hydrochemical and Isotopic (δ2H, δ18O, 3H) Characterization of Fracture Water in Crystalline Rock (Grimsel, Switzerland). *Procedia Earth and Planetary Science*, *17*, 738–741. https://doi.org/10.1016/j.proeps.2016.12.187

Scholz, C. H. (1998). Earthquakes and friction laws. *Nature*, *391*(6662), 37–42. https://doi.org/10.1038/34097

Scholz, C. H. (2019). *The Mechanics of Earthquakes and Faulting* (3rd ed.). Cambridge University Press. https://doi.org/10.1017/9781316681473

Shea, W. T., & Kronenberg, A. K. (1992). Rheology and deformation mechanisms of an isotropic mica schist. *Journal of Geophysical Research: Solid Earth*, *97*(B11), 15201–15237. https://doi.org/10.1029/92JB00620

Sibson, R. H. (1982). Fault zone models, heat flow, and the depth distribution of earthquakes in the continental crust of the United States. *Bulletin of the Seismological Society of America*, *72*(1), 151–163. https://doi.org/10.1785/BSSA0720010151

Simpson, C. (1985). Deformation of granitic rocks across the brittle-ductile transition. *Journal of Structural Geology*, *7*(5), 503–511. https://doi.org/10.1016/0191-8141(85)90023-9

Smith, S. a. F., Strachan, R. A., & Holdsworth, R. E. (2007). Microstructural evolution within a partitioned midcrustal transpression zone, northeast Greenland Caledonides. *Tectonics*, *26*(4). https://doi.org/10.1029/2006TC001952

Spiers, C. J., Schutjens, P. M. T. M., Brzesowsky, R. H., Peach, C. J., Liezenberg, J. L., & Zwart, H. J. (1990). Experimental determination of constitutive parameters governing creep of rocksalt by pressure solution. *Geological Society, London, Special Publications*, *54*(1), 215–227. https://doi.org/10.1144/GSL.SP.1990.054.01.21

Tenthorey, E., Cox, S. F., & Todd, H. F. (2003). Evolution of strength recovery and permeability during fluid–rock reaction in experimental fault zones. *Earth and Planetary Science Letters*, *206*(1), 161–172. https://doi.org/10.1016/S0012-821X(02)01082-8

Tse, S. T., & Rice, J. R. (1986). Crustal earthquake instability in relation to the depth variation of frictional slip properties. *Journal of Geophysical Research: Solid Earth*, *91*(B9), 9452–9472. https://doi.org/10.1029/JB091iB09p09452

Tullis, J., & Yund, R. (1992). Chapter 4 The Brittle-Ductile Transition in Feldspar Aggregates: An Experimental Study. In *International Geophysics* (Vol. 51, pp. 89–117). Elsevier. https://doi.org/10.1016/S0074-6142(08)62816-8

Tullis, J., & Yund, R. A. (1980). Hydrolytic weakening of experimentally deformed Westerly granite and Hale albite rock. *Journal of Structural Geology*, *2*(4), 439–451. https://doi.org/10.1016/0191-8141(80)90005-X

Twiss, R. J., & Moores, E. M. (1992). *Structural geology*. New York: W.H. Freeman.

Verberne, B. A., Niemeijer, A. R., De Bresser, J. H. P., & Spiers, C. J. (2015). Mechanical behavior and microstructure of simulated calcite fault gouge sheared at 20–600°C: Implications for natural faults in limestones. *Journal of Geophysical Research: Solid Earth*, *120*(12), 8169–8196. https://doi.org/10.1002/2015JB012292

Verberne, B. A., Chen, J., Niemeijer, A. R., de Bresser, J. H. P., Pennock, G. M., Drury, M. R., & Spiers, C. J. (2017). Microscale cavitation as a mechanism for nucleating earthquakes at the base of the seismogenic zone. *Nature Communications*, *8*(1), 1645. https://doi.org/10.1038/s41467-017-01843-3

Viegas, L. G. F., Archanjo, C. J., Hollanda, M. H. B. M., & Vauchez, A. (2014). Microfabrics and zircon U–Pb (SHRIMP) chronology of mylonites from the Patos shear zone (Borborema Province, NE Brazil). *Precambrian Research*, *243*, 1–17. https://doi.org/10.1016/j.precamres.2013.12.020

Visser, H. J. M., Spiers, C. J., & Hangx, S. J. T. (2012). Effects of interfacial energy on compaction creep by intergranular pressure solution: Theory versus experiments on a rock analog ($NaNO_3$): EFFECTS OF INTERFACIAL ENERGY ON CREEP. *Journal of Geophysical Research: Solid Earth*, *117*(B11), n/a-n/a. https://doi.org/10.1029/2012JB009590

Wassmann, S., & Stöckhert, B. (2013). Rheology of the plate interface — Dissolution precipitation creep in high pressure metamorphic rocks. *Tectonophysics*, *608*, 1–29. https://doi.org/10.1016/j.tecto.2013.09.030

Weertman, J. (1978). Creep laws for the mantle of the Earth. *Philosophical Transactions of the Royal Society of London. Series A, Mathematical and Physical Sciences*, *288*(1350), 9–26. https://doi.org/10.1098/rsta.1978.0003

Wehrens, P., Berger, A., Peters, M., Spillmann, T., & Herwegh, M. (2016). Deformation at the frictional-viscous transition: Evidence for cycles of fluid-assisted embrittlement and ductile deformation in the granitoid crust. *Tectonophysics*, *693*, 66–84. https://doi.org/10.1016/j.tecto.2016.10.022

Zhang, X., & Spiers, C. J. (2005). Compaction of granular calcite by pressure solution at room temperature and effects of pore fluid chemistry. *International Journal of Rock Mechanics and Mining Sciences*, *42*(7–8), 950–960. https://doi.org/10.1016/j.ijrmms.2005.05.017

Zhang, Xiangmin, Spiers, C. J., & Peach, C. J. (2010). Compaction creep of wet granular calcite by pressure solution at 28°C to 150°C. *Journal of Geophysical Research: Solid Earth*, *115*(B9). https://doi.org/10.1029/2008JB005853

Zwingmann, H., Berger, A., Eggenberger, U., Todd, A., & Herwegh, M. (2017). Testing High-Voltage Electrical Discharges in Disintegrating Claystone for Isotopic and Mineralogical Studies: An Example Using Opalinus Claystone. *Clays and Clay Minerals*, *65*(5), 342–354. https://doi.org/10.1346/CCMN.2017.064072

**References From the Supporting Information**

Akker, I. V., Kaufmann, J., Desbois, G., Klaver, J., Urai, J. L., Berger, A., & Herwegh, M. (2018). Multiscale porosity changes along the pro- and retrograde deformation path: an example from Alpine slates. *Solid Earth*, *9*(5), 1141–1156. https://doi.org/10.5194/se-9-1141-2018

An, M., Zhang, F., Min, K., Elsworth, D., He, C., & Zhao, L. (2022). Frictional Stability of Metamorphic Epidote in Granitoid Faults Under Hydrothermal Conditions and

Implications for Injection-Induced Seismicity. *Journal of Geophysical Research: Solid Earth*, *127*(3), e2021JB023136. https://doi.org/10.1029/2021JB023136

Berg, S., Kutra, D., Kroeger, T., Straehle, C. N., Kausler, B. X., Haubold, C., et al. (2019). ilastik: interactive machine learning for (bio)image analysis. *Nature Methods*, *16*(12), 1226–1232. https://doi.org/10.1038/s41592-019-0582-9

Blanpied, M. L., Lockner, D. A., & Byerlee, J. D. (1995). Frictional slip of granite at hydrothermal conditions. *Journal of Geophysical Research: Solid Earth*, *100*(B7), 13045–13064. https://doi.org/10.1029/95JB00862

Dinnebier, R. E., & Billinge, S. J. L. (Eds.). (2008). *Powder diffraction: theory and practice*. Cambridge: Royal Society of Chemistry.

Kanit, T., Forest, S., Galliet, I., Mounoury, V., & Jeulin, D. (2003). Determination of the size of the representative volume element for random composites: statistical and numerical approach. *International Journal of Solids and Structures*, *40*(13–14), 3647–3679. https://doi.org/10.1016/S0020-7683(03)00143-4

Lei, H., Zhou, Y., Yao, W., Ma, X., He, C., Dang, J., et al. (2022). Earthquake nucleation conditions of Anninghe Fault constrains from frictional experiments on natural granite gouge. *Chinese Journal of Geophysics*, *65*(3), 978–991. https://doi.org/10.6038/cjg2022P0248

Lockner, D. A., & Byerlee, J. D. (1986). *Open File Report* (Open-File Report).

Mitchell, E. K., Fialko, Y., & Brown, K. M. (2016). Velocity-weakening behavior of Westerly granite at temperature up to 600°C. *Journal of Geophysical Research: Solid Earth*, *121*(9), 6932–6946. https://doi.org/10.1002/2016JB013081

Okuda, H., Niemeijer, A. R., Takahashi, M., Yamaguchi, A., & Spiers, C. J. (2023). Hydrothermal Friction Experiments on Simulated Basaltic Fault Gouge and

Implications for Megathrust Earthquakes. *Journal of Geophysical Research: Solid Earth*, *128*(1), e2022JB025072. https://doi.org/10.1029/2022JB025072

Rietveld, H. M. (1969). A profile refinement method for nuclear and magnetic structures. *Journal of Applied Crystallography*, *2*(2), 65–71. https://doi.org/10.1107/S0021889869006558